OPTIMIZATION PARAMETERS FOR A MEMBRANE POLYGONAL BODY OF REVOLUTION WITH ZERO MERIDIONAL STRESS AND ITS APPLICATION TO PARACHUTES

By

John L. Gilbert

Thesis submitted to the Graduate Faculty of the
Virginia Polytechnic Institute and State University
in the candidacy for the degree of
DOCTOR OF PHILOSOPHY

in

Aerospace Engineering

Approved:

Chairman, F. H. Lutze

E. M. Cliff

H. L. Johnson

D. Frederick

T. A. Weisshaar

June 1974

Blacksburg, Virginia

LD
5655
V856
1974
G55
c.2

TABLE OF CONTENTS

Page

TITLE i

TABLE OF CONTENTS ii

ACKNOWLEDGEMENTS. iv

LIST OF FIGURES v

SYMBOLS vii

INTRODUCTION. 1

1. FUNDAMENTAL STRUCTURAL EQUATIONS. 8

1.1 Geometric Equations and Kinematic Relations for Secondary Membrane Structure 8

1.2 Equilibrium Equations for Membrane Structure 12

1.3 Equilibrium Equations for Meridional Members 14

1.4 Coordinate Transformation. 17

1.5 Governing Equations for Polygonal Structure. 22

2. SOLUTIONS TO EQUATIONS FOR POLYGONAL SHAPES 27

2.1 Solution for Given Gore Shapes 31

2.2 Analysis of Existing Parachutes Input Data 32

2.2.1 Material Properties and Pressure Coefficients . . 32

2.2.2 Geometry of Existing Parachutes 39

2.2.3 Results and Discussion. 42

3. OPTIMIZATION EQUATIONS. 50

3.1 Necessary Conditions 52

Page

4. SOLUTION OF OPTIMIZATION EQUATIONS 58

4.1 Solution Using the Maximum Principle. 59

4.1.1 Solution of State Equations. 63

4.2 Rayleigh-Ritz Method. 69

4.3 Steepest Descent Solution 72

4.4 Results and Discussion. 78

5. COMPARISON OF OPTIMIZED WITH EXISTING PARACHUTES 86

5.1 Comparison of Shapes. 87

5.2 Major Influencing Parameters. 89

5.3 Results and Discussions 98

6. CONCLUSIONS. 100

7. REFERENCES 104

APPENDIX A - SOLUTION OF THE THETA TRANSCENDENTAL EQUATION . 107

ACKNOWLEDGEMENTS

The author wishes to express his thanks to the National Aeronautics and Space Administration for permitting this work to be performed as part of the author's work assignment at the Langley Research Center. He would like to express his thanks to Mr. Kenneth Bush, of the Langley Research Center, for the initial encouragement in this problem and Dr. Fred H. Lutze, of Virginia Polytechnic Institute and State University, for his counsel and guidance. Finally, the author wishes to thank his wife, Doris, and his children, Gregory and Cynthia, for their patience and understanding during the course of this research program.

LIST OF FIGURES AND TABLES

Figure Page

1. Parachute structural members 7
2. Differential element of a gore 11
3. Differential element of primary member 14
4. Coordinate system of differential element. 17
5. Global coordinate system 18
6. Parachute program flow diagram 33
7. Pressure distribution - variable S. 36
8. Pressure distribution - variable ϕ. 37
9. Flat circular parachute. 39
10. Extended skirt parachute 40
11. Conical parachute. 41
12. 1/4 spherical parachute. 41
13. Comparison of constructed, calculated, and measured canopy profile 43
14. Comparison of calculated membrane stress with reference 31 44
15. Comparison parachute drag coefficient. 46
16. Maximum drag control policy. 69
17. Main program Rayleigh-Ritz method. 72
18. Subroutines for Rayleigh-Ritz method 74
19. Steepest descent flow diagram. 79
20. Convergence of steepest descent. 83
21. Deployed shapes 88
22. Comparison of gore shapes. 99

Figure Page

23. Effect of pressure distribution on control variable . . . 91

24. Effect of pressure distribution on gore shape 92

25. Effect of pressure distribution on deployed shape 93

26. Effect of membrane stiffness on drag 94

27. Effect of skirt angle on suspension line length 95

28. Effect of skirt angle on drag coefficient 97

29. Radial tape strain. 98

30. Gore geometric relations. 110

TABLES

1. Comparison of Calculated and Measured Parachute Membrane Stresses. 45

2. Comparison of Steepest Descent With Rayleigh-Ritz 85

3. Drag Coefficient of the Optimized Parachute Compared With Existing Designs 86

SYMBOLS

A, B	end points of the differential element
a	distance from origin to membrane coordinates (see fig. 2)
C	terms in the constituate matrix
C_D	drag coefficient
c	constraint equation constant
c_p	pressure coefficient
c_{p_i} $_{i=1,4}$	coefficients of pressure polynomial
D	width of gore
D_o	undeformed gore width
E_{cc}	Young's modulus of membrane in the circumferential direction
E, F, G	first fundamental magnitudes
E_{RT}	Young's modulus of the meridional tapes
$E_{\theta\theta}$, $E_{\phi\phi}$	Young's modulus of the orthotropic material
N_{x_2}, N_{y_2}, N_{z_2}	stress resultants in the element coordinate system
f	differential equation function
H	Hamiltonian
J	performance index
K_1	meridional curvature
K_2	circumferential curvature
k	constant for steepest descent
L, M, N	second fundamental magnitudes

L_S	suspension line length
l	distance between chords
N	number of gores
N_θ	circumferential stress
N_ϕ	meridional stress
$N_{\theta\phi}$	shear stress
N_{X_2}, N_{Y_2}, N_{Z_2}	stress resultants in the membrane coordinate system
p	pressure normal to the surface
Q	dynamic pressure
R	radius of the deformed element
R_ϕ	chord radius curvature
r	radius of curvature of the membrane structure
$\vec{r}$	vector to membrane surface
S	meridional distance
S_{TR}	stretch of the chord
T	chord force
$[T]$	coordinate transformation matrix
T_R	reference force
u	meridional displacement
V_i	coefficients of series expansion of the control variable
v	circumferential displacement
w	displacement in the direction of the position vector

x_1, y_1, z_1	coordinates in the meridional primary structure
x_2, y_2, z_2	coordinates in the intrinsic system
Z	axial distance of the deformed element
α	orientation of the orthotropic material
β	angular measurement between gores
$\gamma_{\phi\theta}$	shear strain
ε_θ	strain in the hoop direction
ε_ϕ	strain in the meridional direction
L	differential distance
η	performance variable
θ	circumferential coordinate of membrane
$\bar{\theta}$	theta measured at primary member
λ	adjoint variables
$\nu_{\theta\phi}$	Poisson's ratio
ξ	axial distance to the undeformed element
λ_r	ratio of r/a
μ	multiplier in Hamiltonian
ρ	radius to undeformed element
ϕ	meridional coordinate
Φ	objective function
ψ	constraint equation

INTRODUCTION

Drag devices used for recovering aerospace vehicles such as balloons, ballutes, and parachutes are typically made with discretely spaced tapes joined by some fabric membrane material. Loads in the meridional direction are carried by the tapes which are designated as primary members, while pressure loads are transferred to these tapes by the membrane or so-called secondary members. Construction consists of an assembly of fabric polygons for the secondary members joined to the meridional tapes which are distributed about an axis of symmetry. Hence, the term polygonal body of revolution (ref. 30) is used to describe these devices. An example of such a drag device is the parachute which is illustrated in figure 1 with the various structural components identified. The object of this research is to analytically determine the shape of the membrane polygons which will make these devices (parachute) more efficient by increasing the drag, drag coefficient, and at the same time reducing the area.

Numerous factors influence the design of these type structures, so it is necessary to identify the important parameters and develop design procedures based on sound theoretical consideration rather than expensive trial and error programs currently in use. The results of some previous papers dealing with theoretical and experimental design procedures developed to date are discussed.

A primary concern in the design of drag devices is the strength needed to survive deployment loads since maximum stresses usually occur

during this phase. Consequently, much of the research effort in decelerator design has been devoted to predicting structural loads, with the resulting studies suggesting the desirability of optimized designs. For example, in reference 22, a fully stressed isotensoid design ballute is derived, and in references 30, 32, and 33, parachutes with optimized stress distributions are discussed.

In contrast, existing literature on optimizing drag performance is very meager. In the early work in parachute designs, Taylor (ref. 33) and later Stevens and Johns (ref. 32) proposed an analytically derived maximum drag design. Studies in the current literature usually are more concerned with drag at a system level, where the drag characteristics of various parachutes are taken from test data and become one of many parameters in the selection of an acceptable design. An important parameter in an effective drag design is the shape of the secondary member, or for a parachute, this would be the gore shape. Numerous shapes have been developed, the most common being a trapezoidal polygon, which upon assembling generates a parachute that approaches a flat circular disk; hence, the name flat circular has been used in the vernacular of the parachute industry. Variations of this design have resulted in parachute designs such as extended skirt, conical, bi-conical, shape gore, and one-quarter hemisphere. A more detailed discussion of the influence of gore shapes is discussed in reference 3. In this reference a qualitative evaluation of various gore shapes such as conical, flat circular, and extended skirt is presented. The results are derived from test data and no analytical

verification attempted.

Numerous studies have been conducted for decelerator development, the earliest being the analytical work of the British investigators Taylor, Southwell, Griffiths, Jones, and Williams at the Royal Aircraft Establishment in 1919. This work was summarized by Jones and published in 1919 in which he presented the Taylor shape that is familiar to parachute designers. This fundamental analysis was further studied by Stevens and Johns (ref. 32). In this reference the treatment of loading on the secondary member, or canopy cloth, was quite different from Taylor's, although the final results were identical.

Taylor studied an axisymmetric parachute with a large number of primary meridional members (radial tapes) and concluded that the bulges between the tapes could be removed as the number became very large. This would be the flatest possible chute, he reasoned, and therefore would be of minimum weight (refs. 32 and 33).

Stevens and Johns (ref. 32) conducted research on parachutes with shorter tapes over the canopy and published the results in 1942. By making the tape shorter, it was assumed that the meridional stresses would be zero and all of the pressure loads would be carried in the hoop direction. An erroneous assumption was made in the derivation which resulted in radial tapes having constant load. Thus, Stevens and Johns obtained the same results as Taylor from quite different assumptions. Although the Taylor curve was a gross approximation, it remained one of the fundamental shapes for analytical purposes until

the mid-50's.

In fact, it was used extensively in the report by Topping, Mankotes, and Costakos (ref. 34) published in 1955. This report was quite an advancement over the papers that had been published at that time. In 1962, Lester (ref. 26) modified the Taylor shape by including a parameter for generating a family of curves.

Heinrich, et al. (ref. 18) developed an iterative solution for arriving at equilibrium conditions from photographs of observed shapes with known pressure distributions. This method is also presented in the "Parachute Handbook" (ref. 3) and is used extensively for stress calculations.

Mullins (ref. 30) of Northrop Ventura developed a finite element solution for the Apollo spacecraft parachute. A computer solution was obtained and agreement with test data was good. Mullins states in this report that an optimum parachute design; that is, overall maximum stress, could be obtained by an extension of this program.

An analysis of a flat circular parachute under steady-state descent conditions was accomplished by Ross in reference 31. He presents the solution to a third-order nonlinear ordinary differential equation by use of the Runge-Kutta integration method. The study made by Ross is similar to that of Heinrich in reference 18, although the derivations are more rigorous and he extends the work of Heinrich.

An energy approach to the parachute opening dynamics problem was first proposed by Asfour (ref. 6). This was a new approach in which the canopy circumferential strain energy is assumed to be equal to the

energy of the air mass expanding and filling the canopy during inflation. Houmard (ref. 21) extended this approach by making it more general and programed for a numerical solution on the computer. This method was applied to the Viking Project parachute design.

Other types of decelerator structures include such things as ballutes and balloons. Ballutes were analyzed and reported by Houtz in reference 22. In this paper the primary stresses were in the meridional direction only, and a constant percentage of this stress was assumed to act in the circumferential direction. This approach was modified to include a surface with constant orthotropic stress. The term "isotensoid" was given to this type of structure and was said to be optimized since the material was fully utilized.

For the optimum drag design, some of the design innovations include such things as extended skirt design, pull down vent, shaped gore, guided surface, and bi-conical to only mention a few. These designs were arrived at by trial and error and represent much effort in research and development resources. Apparently, no analytical means were used to optimize designs as is sometimes done for stress distributions. It is the purpose of this research to show some of the major factors influencing an optimum design for maximum drag and drag coefficients. A comparison is made with current parachute designs.

This study is limited to structures with zero membrane stress in the secondary members, and thus, the double curvature can be approximated with short segments that are developable. Surfaces with zero Gaussian curvature are said to be developable since an initially

flat surface can be used in its construction. Wrinkling can occur when a flat surface is required to conform to a doubly curved shell. This subject was studied extensively by Mikulas, reference 28. Research on a typical developable surface, the Rogallo parawing, is presented in reference 15. A basic assumption used throughout the work presented in this dissertation is that the flat surface will be deformed to a double curvature without wrinkling, a fact that has been observed in numerous tests.

The object of this study is to optimize the drag and drag coefficient by determining the desired shape of the gore subject to the previously defined condition that the secondary membrane meridional stress be zero. This condition is assured by designing the primary members shorter than the secondary membrane structure. Other factors such as opening characteristics and dynamic stability are primary influences on the design but are not considered directly in this study.

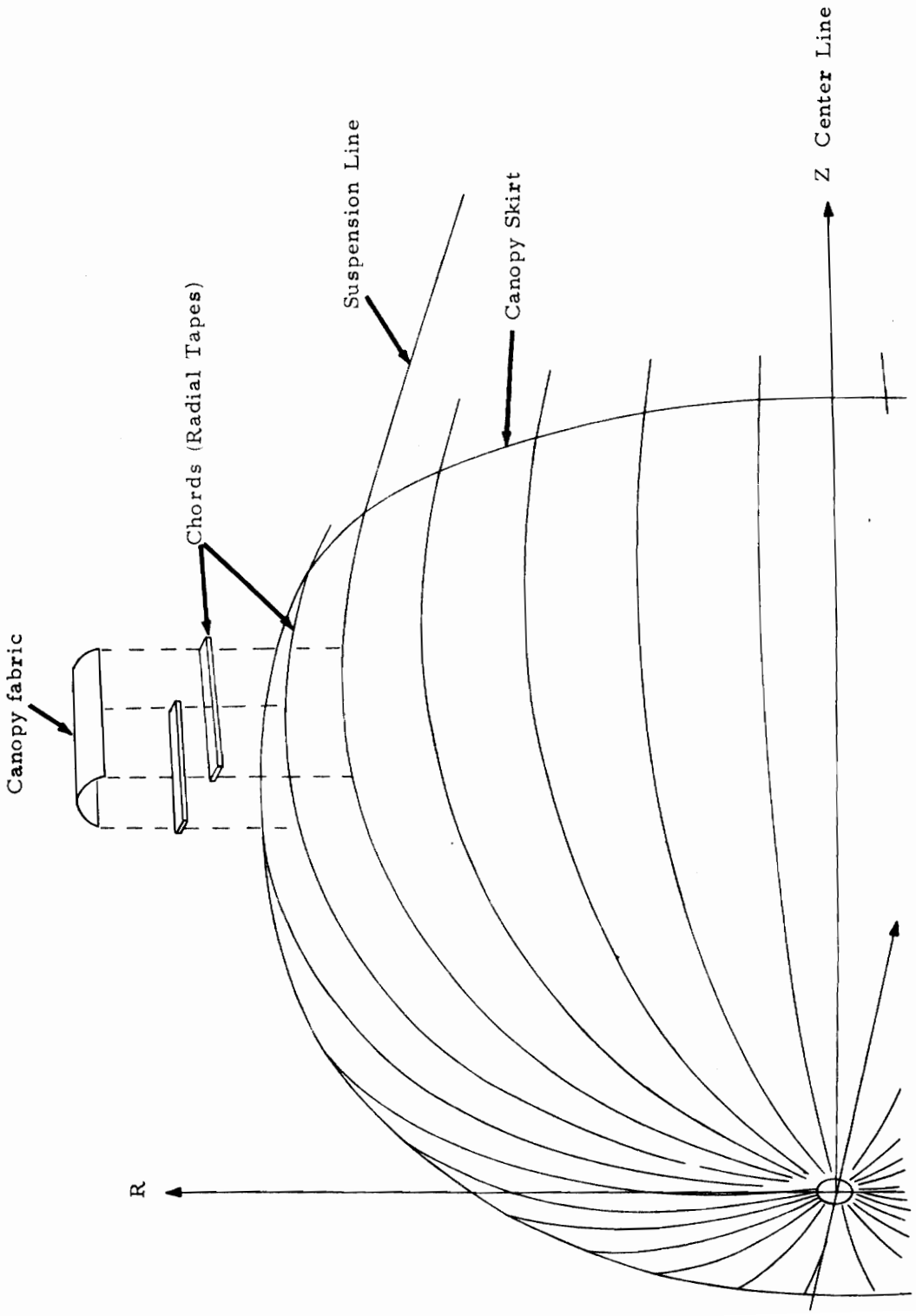

Figure 1.- Parachute structural members

1. FUNDAMENTAL STRUCTURAL EQUATIONS

Derivations of the fundamental equations for the secondary membrane structure and primary meridional structure are presented in this section. The membrane structure is divided into discrete segments that can be approximated by a developable surface. Meridional and shear stresses in the membrane are assumed to be negligibly small because of the special type structure considered. Loads from the secondary structure are transformed to an intrinsic coordinate system defined along the primary structure where the coordinates are measured tangent and normal to the member. Large deflections are considered in the derivation of the equilibrium equations for the primary member.

1.1 Geometric Equations and Kinematic Relations for Secondary Membrane Structure

The doubly curved surface shown in figure 2 is defined by the coordinates ϕ, θ, or in terms of Cartesian coordinates with origin at the center of the primary member curvature

$$x_1 = r \sin \theta$$

$$y_1 = (a + r \cos \theta) \cos \phi \qquad (1)$$

$$z_1 = (a + r \cos \theta) \sin \phi$$

where r is constant. Writing equation (1) as a vector

$$\vec{r} = \vec{i}\, r \sin\theta + \vec{j}\,(a + r\cos\theta)\cos\phi + \vec{k}(a + r\cos\theta)\sin\phi \qquad (2)$$

The square of the differential distance is

$$d\zeta^2 = r^2\, d\theta^2 + a^2\,(1 + \lambda_r \cos\theta)^2\, d\phi \qquad (3)$$

where

$$\lambda_r = r/a$$

from which the first fundamental magnitudes are found

$$E = r^2$$

$$F = 0 \qquad (4)$$

$$G = a^2\,(1 + \lambda_r \cos\theta)^2$$

and the second fundamental magnitudes are

$$L = -\frac{\partial^2 \vec{r}}{\partial^2 \theta} \cdot \vec{\eta} = r$$

$$M = -\frac{\partial^2 \vec{r}}{\partial\phi\partial\theta} \cdot \vec{\eta} = 0 \qquad (5)$$

$$N = -\frac{\partial^2 \vec{r}}{\partial^2 \phi} = a\,(1 + \lambda_r \cos\theta)\cos\theta$$

where $\vec{n}$ is a unit vector normal to the surface; positive when pointing from the concave side to the convex side.

The curvatures are found from the expressions

$$K_1 = \frac{L}{E} = \frac{1}{r}$$

$$K_2 = \frac{N}{G} = \frac{\cos\theta}{a\,(1 + \lambda_r \cos\theta)} \tag{6}$$

During the angle change $d\phi$, the meridional direction curvature (o-a) is assumed to remain constant, and since the incremental change is limited to small angles, the primary structure is approximated with parallel members. The general strain-displacement relations for the membrane are (ref. 21)

$$\varepsilon_\theta = \frac{1}{r}\frac{\partial v}{\partial\theta} + \frac{u}{ar(1 + \lambda_r \cos\theta)}\frac{\partial r}{\partial\phi} + \frac{\omega}{r}$$

$$\varepsilon_\phi = \frac{1}{a(1 + \lambda_r \cos\theta)}\left(\frac{\partial u}{\partial\phi} + \omega\cos\theta\right) + \frac{v}{ar(1 + \lambda_r \cos\theta)}\frac{\partial a(1 + \lambda_r \cos\theta)}{\partial\theta} \tag{7}$$

$$\gamma_{\theta\phi} = \frac{a(1 + \lambda_r \cos\theta)}{r}\frac{\partial}{\partial\theta}\left(\frac{u}{a(1 + \lambda_r \cos\theta)}\right) + \frac{r}{a(1 + \lambda_r \cos\theta)}\frac{\partial v/r}{\partial\phi}$$

The following basic assumptions were made to simplify the problem: meridional members carry all of the meridional load, the radius a is very large and consequently λ_r small, both r and a are constant, membrane stress in hoop direction only, and the bulge

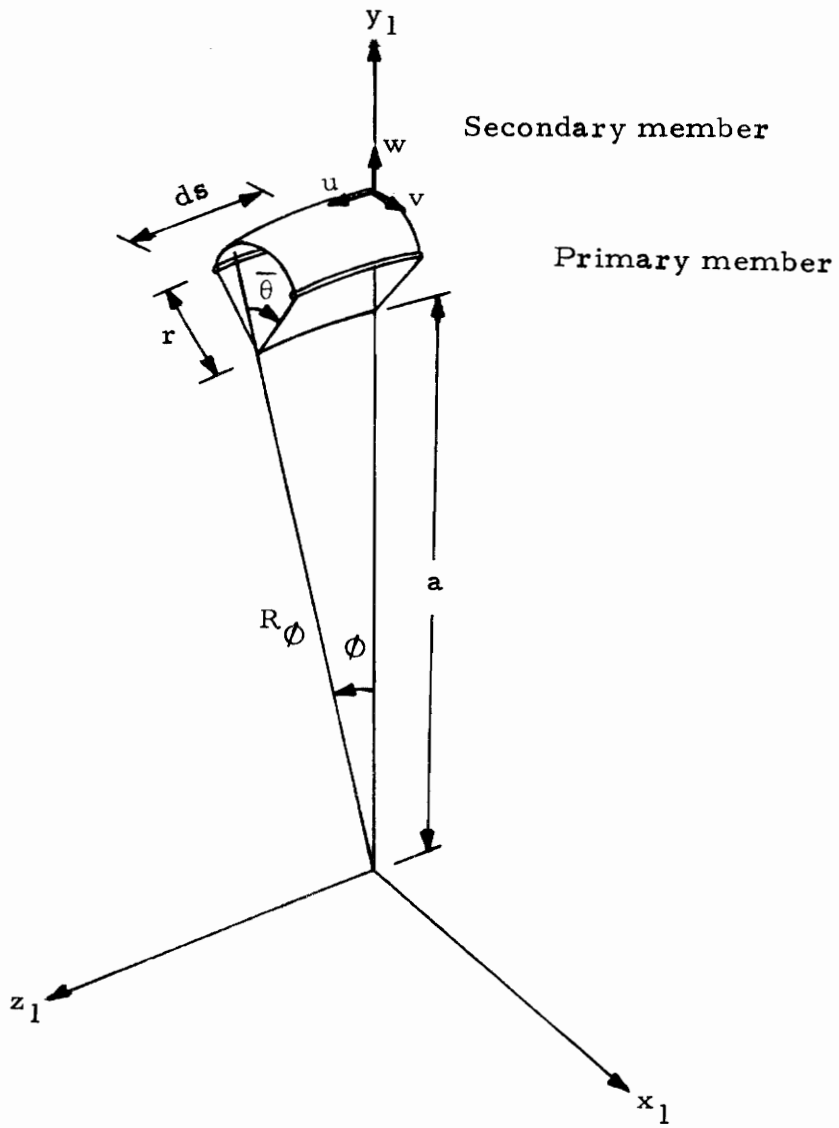

Figure 2.- Differential element of gore.

between the primary members stretches uniformly.

Considering the strain in the hoop direction, the first term is negligible since the stretch is assumed uniform, and the second term is zero as r is constant. For the meridional strain, ε_ϕ is zero since there is no stretching in the meridional direction and a is large. Shear strain is negligible since the stretching is assumed to be zero in the meridional direction and uniform in the hoop direction. Applying these conditions leaves only one term of significance, that is

$$\varepsilon_\theta = \frac{\omega}{r} \tag{8}$$

1.2 Equilibrium Equations for Membrane Structure

The general membrane equilibrium equations are derived in reference 23 in terms of the fundamental quantities and magnitudes. Applying these equations to the geometry described in the previous section results in the three equilibrium equations for the secondary structure. For the case with pressure applied normal to surface, these equations are

$$\frac{\partial}{\partial\theta}\left(N_\theta\, a(1+\lambda_r\cos\theta)\right) + \frac{\partial}{\partial\phi}\left(N_{\theta\phi}\, r\right) + N_{\theta\phi}\frac{\partial r}{\partial\phi} - N_\phi\frac{\partial a(1+\lambda_r\cos\theta)}{\partial\theta} = 0$$

$$\frac{\partial}{\partial\theta}\left(N_{\theta\phi}\, a(1+\lambda_r\cos\theta)\right) + \frac{\partial}{\partial\phi}\left(N_\phi\, r\right) + N_{\theta\phi}\frac{\partial a(1+\lambda_r\cos\theta)}{\partial\theta} - N_\theta\frac{\partial r}{\partial\phi} = 0 \tag{9}$$

$$\frac{N_\theta}{r} + \frac{N_\phi\cos\theta}{a(1+\lambda_r\cos\theta)} = p$$

For low pressures, the shear rigidity of fabric type materials is low (ref. 2), and consequently, the shear stress considered negligible. The same assumptions used for reducing the strain relations also apply for the equilibrium equations. By neglecting meridional and shear stresses and assuming uniform stretching, the first equation is negligible, and the second equation can be omitted if the meridional and shear stresses are small. Finally, the last equation reduces to two terms when considering a large; therefore

$$N_\theta = pr = \text{constant} \tag{10}$$

where p is the normal pressure and r is the curvature of the membrane.

Since only one stress resultant is involved, the stress-strain relationships reduce to

$$\varepsilon_\theta = \frac{N_\theta}{E_{cc}} \tag{11}$$

where E_{cc} is Young's modulus in the hoop direction multiplied by the thickness.

The final outcome of these assumptions is to reduce the doubly curved element to a cylindrical element with hoop stresses only. While other approximations could be made, it is felt, for practical applications, these are reasonable and agree well with test results, (ref. 20).

1.3 Equilibrium Equations for Meridional Members

The primary members receive the circumferential forces and serve to transfer the resultant loads to the boundaries, whereas, internal applied pressure forces are carried solely by the secondary membrane structure. Primary structure consists of tapes that span in the meridional direction from the vent to the skirt. Large strains are included in the equilibrium equations due to large influence of stretching for this type of structure. Both deformed and undeformed differential elements are shown in figure 3, (ref. 14).

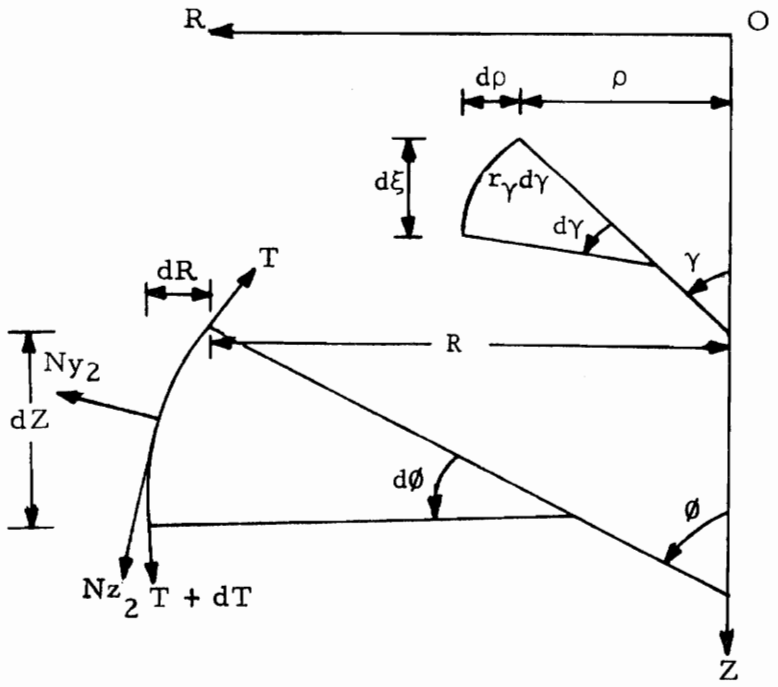

Figure 3.- Differential element of primary member.

Summing the stress resultants parallel to the axis of revolution requires that

$$-T \sin \phi + [T + dT] \sin (\phi + d\phi) - (N_{y_2} \cos \phi - N_{z_2} \sin \phi) r_\phi \, d\phi = 0$$

and dropping products of higher order terms gives

$$\frac{d}{d\phi} (T \sin \phi) = (N_{y_2} \cos \phi - N_{z_2} \sin \phi) r_\phi \tag{12}$$

and equilibrium in the radial direction requires

$$-T \cos \phi + (T + dT) \cos (\phi + d\phi) + (N_{y_2} \sin \phi + N_{z_2} \cos \phi) r_\phi \, d\phi \tag{13}$$

which upon dropping products gives

$$\frac{d}{d\phi} (T \cos \phi) = - (N_{y_2} \sin \phi + N_{z_2} \cos \phi) r_\phi \tag{14}$$

From the geometry of the undeformed element, we see that

$$r_\phi \, d\phi = (1 + \varepsilon_\phi) r_\gamma \, d\gamma \tag{15}$$

where

$$\varepsilon_\phi = T/E_{RT}$$

is the strain in the primary member in the meridional direction. The stretch in the chord is given by

$$S_{TR} = (1 + T/E_{RT})$$

then multiplying equation (12) by $\sin \phi$ and (13) by $\cos \phi$ and first adding and then multiplying equation (12) by $\cos \phi$ and (13) by $\sin \phi$ and subtracting the following intrinsic equilibrium equations result:

$$dT/dS = -N_{z_2} S_{TR} \tag{16}$$

and

$$d\phi/dS = N_{y_2} S_{TR}/T$$

where

$$dS = r_\gamma \, d\gamma \tag{17}$$

is the undeformed differential distance in the meridional direction. Coordinates of the undeformed elements are determined from

$$d\rho = r_\gamma \, d\gamma \cos \gamma$$

$$d\xi = r_\gamma \, d\gamma \sin \gamma \tag{18}$$

and the coordinates of the deformed elements are

$$dR/dS = \cos \phi \; S_{TR}$$

$$dZ/dS = \sin \phi \; S_{TR} \tag{19}$$

1.4 Coordinate Transformation

Membrane stress resultants of the secondary structure are transformed to an intrinsic coordinate system located in the meridional members such that the axes are tangent and perpendicular to the primary member. By making this transformation, the membrane stress resultants can readily be summed for use in the equilibrium differential equations of the primary member. The local coordinate system of the membrane element is shown in figure 4. In order to simplify derivations to follow, points A and B were selected to be on the x_1 axis with point A at the origin.

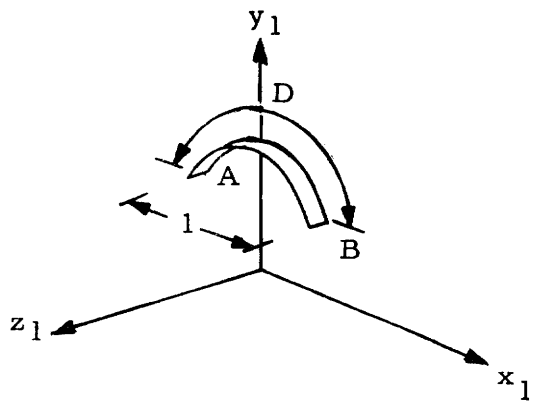

Figure 4.- Coordinate system of differential elements.

Next, the differential element system is combined with the primary member coordinate system. An intermediary system, or global coordinates, are used to facilitate this step.

The element in the global coordinate system is shown in figure 5.

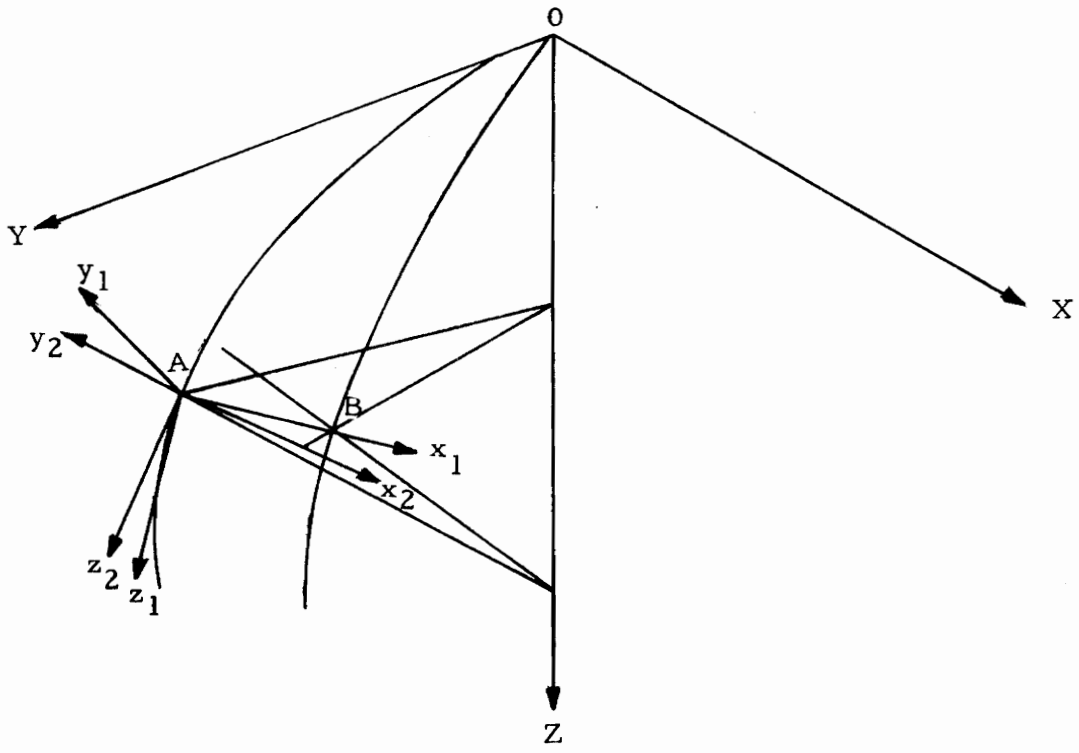

Figure 5.- Global coordinate system.

Certain geometric conditions are obvious for a polygonal type structure. The line AB has to be in a plane parallel to the XY plane, and since the meridian containing A was arbitrarily selected to be in the YZ plane, then AB is not parallel to the XZ plane but pointing toward it by an angle π/N radians. Since the membrane is assumed to have no shear loads, then it must lie in the plane

defined by the line AB and a perpendicular to a tangent of the meridional member at point A; in other words, coordinate y_2. The coordinate z_1 has to be normal to the y_2, AB plane, and the y_1 coordinate is determined by the vector cross product. Unit vectors in this system can be written

$$\begin{aligned} \vec{I}_{x_1} &= \vec{i} \cos \pi/N - \vec{j} \sin \pi/N \\ \vec{I}_{y_2} &= \vec{j} \sin \phi - \vec{k} \cos \phi \end{aligned} \tag{20}$$

where $\vec{i}$, $\vec{j}$, $\vec{k}$, are unit vectors in the global system and the vector product gives

$$\vec{I}_{z_1} = \cos \beta(\vec{i} \cos \phi \sin \pi/N + \vec{j} \cos \phi \cos \pi/N + \vec{k} \cos \pi/N \sin \phi) \tag{21}$$

where β is the angle between y_1 and y_2 and is defined as

$$\sin \beta = \sin \pi/N \sin \phi \tag{22}$$

and the coordinate base vector on z_1 is found from the vector cross product

$$\vec{I}_{y_1} = \vec{i} \cos \pi/N \tan \beta + \vec{j} \cos^2 \pi/N \sin \phi/\cos \beta - \vec{k} \cos \phi/\cos \beta \tag{23}$$

The transformation from the global coordinates to the secondary membrane coordinate system is

$$\begin{Bmatrix} x_1 \\ y_1 \\ z_1 \end{Bmatrix} = \begin{bmatrix} \cos \pi/N & -\sin \pi/N & 0 \\ \cos \pi/N \tan \beta & \cos^2 \pi/N \sin \phi/\cos \beta & -\cos \phi/\cos \beta \\ \cos \phi \sin \pi/N/\cos \beta & \cos \phi \cos \pi/N/\cos \beta & \cos \pi/N \sin \phi/\cos \beta \end{bmatrix} \begin{Bmatrix} X \\ Y \\ Z \end{Bmatrix} \tag{24}$$

Next, the intrinsic coordinate system x_2, y_2, z_2 is defined in terms of the XYZ system. This system is defined such that z_2 is tangent to the meridian at point A, y_2 is perpendicular to z_2 and lies in the XZ plane, and x_2 is orthogonal to y_2 and z_2. Thus the transformation is given by

$$\begin{Bmatrix} x_2 \\ y_2 \\ z_2 \end{Bmatrix} = \begin{bmatrix} 1 & 0 & 0 \\ 0 & \sin \phi & -\cos \phi \\ 0 & \cos \phi & \sin \phi \end{bmatrix} \begin{Bmatrix} X \\ Y \\ Z \end{Bmatrix} \tag{25}$$

Equation (24) can be inverted to solve for the global coordinates, and the resulting expression substituted in equation (25), which gives the transformation from the membrane coordinate system to the primary meridional members.

$$\begin{Bmatrix} x_2 \\ y_2 \\ z_2 \end{Bmatrix} = \begin{bmatrix} \cos \pi/N & \cos \pi/N \tan \beta & \cos \phi \sin \pi/N/\cos \beta \\ -\sin \beta & \cos \beta & 0 \\ -\cos \phi \sin \pi/N & -\cos \phi \sin \pi/N \tan \beta & \cos \pi/N/\cos \beta \end{bmatrix} \begin{Bmatrix} x_1 \\ y_1 \\ z_1 \end{Bmatrix} \tag{26}$$

Similarly, the stress resultant transformation has the same expression, and since only the hoop stress is being considered, from equation (10)

$$\begin{Bmatrix} N_{x_2} \\ N_{y_2} \\ N_{z_2} \end{Bmatrix} = [T] \begin{Bmatrix} pr \cos \bar{\theta} \\ pr \sin \bar{\theta} \\ 0 \end{Bmatrix} \tag{27}$$

where $[T]$ is the transformation matrix in equation (26), and the stress resultants are evaluated at the tape where $\theta = \bar{\theta}$.

The curvature of the membrane r can be determined from the geometry shown in figure 30 of Appendix A. Therefore

$$r = R \sin \pi/N / \sin \bar{\theta} \tag{28}$$

Substituting this expression into equation (27) and performing the matrix product results in the equations

$$\begin{aligned} N_{x_2} &= pR \sin \pi/N \cos \pi/N (\cos \beta \cos \bar{\theta} + \sin \bar{\theta} \sin \beta) \\ N_{y_2} &= pR \sin \pi/N (-\sin \beta \cos \bar{\theta} + \cos \beta \sin \bar{\theta})/\sin \bar{\theta} \\ N_{z_2} &= -pR \sin^2 \pi/N \cos \phi (\cos \bar{\theta} + \sin \bar{\theta} \tan \beta)/\sin \bar{\theta} \end{aligned} \tag{29}$$

These equations can be compared directly with the expressions presented

in reference 30 after some trigonometric substitutions and represent the stress resultants applied to the primary member by the membrane. The first equation N_{x_2} is equilibrated with an opposing force about the primary member due to symmetry and is not required in the equilibrium equations. It is used to specify the maximum angle $\bar{\theta}$ since the hoop force would be zero and therefore unstable when

$$\bar{\theta} \geq \pi/2 + \beta \tag{30}$$

It will be shown later in the optimization section that the limits imposed on this upper boundary greatly influence results of the numerical solution.

1.5 Governing Equations for Polygonal Structure

The primary and secondary equilibrium equations are combined to give the differential equations used to analyze the structure, and become state variable differential equations in the formulation of the optimization problem.

The transformed stress resultants from the secondary members, equation (29), can be substituted into the primary member equilibrium differential equations where a factor of two is applied to account for loads being supplied from each side. Only two equilibrium equations are required; a tangential and a normal equation determine the necessary forces. Combining equations (16) and (29) gives the following

$$\frac{d\phi}{dS} = 2\ pR \sin \pi/N\ (\cos \beta \sin \bar{\theta} - \sin \beta \cos \bar{\theta})\ S_{TR}/T \sin \bar{\theta} \tag{31}$$

$$\frac{dT}{dS} = 2\ pR \sin 2\pi/N \cos \phi\ (\cos \bar{\theta} + \sin \bar{\theta} \tan \beta)\ S_{TR}/\sin \bar{\theta} \tag{32}$$

The pressure is defined by the expression

$$p = C_p\ Q \tag{33}$$

where Q is the dynamic pressure and C_p is defined by the expression

$$C_p = (p_i - p_o)/Q \tag{34}$$

p_i is the local inside pressure and p_o the local outside pressure; both are measured at the surface of the structure.

It is convenient to represent the variation of the pressure coefficient by a series expansion in terms of the independent variable S

$$C_p = C_{p_1} + C_{p_2} S + C_{p_3} S^2 + \text{----}$$

Normalizing by factoring the coefficient C_{p_1} and dividing the variable S by its maximum value S_L gives

$$\bar{C}_p = \left(1 + \frac{C_{p_2}}{C_{p_1}} \bar{S} + \frac{C_{p_3}}{C_{p_1}} \bar{S}^2 + \text{-------}\right) \tag{35}$$

Substituting equations (33) and (35) into equations (31) and (32), nondimensionalizing and simplifying the trigometric expressions gives

$$\frac{d\phi}{d\bar{S}} = 2\bar{R} \sin(\bar{\theta} - \beta)\, \bar{S}_{TR} \left(1 + \frac{C_{p_2}}{C_{p_1}} \bar{S} + \frac{C_{p_3}}{C_{p_1}} \bar{S}^2 + \text{----}\right) \tag{36}$$

and

$$\frac{d\bar{T}}{d\bar{S}} = 2\bar{R} \sin \pi/N \cos\theta\, \bar{S}_{TR} \cos(\bar{\theta} - \beta) \left(1 + \frac{C_{p_2}}{C_{p_1}} \bar{S} + \frac{C_{p_3}}{C_{p_1}} \bar{S}^2 + \text{--}\right) / \sin\bar{\theta} \cos\beta \tag{37}$$

where the nondimensional variables are defined as

$$\bar{T} = T/C_{p_1}\, Q \sin \pi/N\, S_L^2$$

$$\bar{R} = R/S_L$$

$$\bar{S} = S/S_L \tag{38}$$

$$\bar{S}_{TR} = 1 + \bar{T}/\bar{E}_{RT}$$

$$\bar{E}_{cc} = E_{cc}/C_{p_1}\, Q \sin \pi/N\, S_L$$

The two additional equations needed to completely define the structure are given by equation (19). When nondimensionalized they become

$$d\bar{R}/d\bar{S} = \cos \phi \; \bar{S}_{TR} \tag{39}$$

$$d\bar{Z}/d\bar{S} = \sin \phi \; \bar{S}_{TR} \tag{40}$$

In order to obtain a solution to these equations, an additional expression defining the angle θ is needed. From the equations for the strain in the hoop direction, the secondary membrane strain is given by equation (8) or

$$\omega = \varepsilon_{\theta} r \tag{41}$$

From the geometric relationship between the constructed gore width and distance between the primary members, and considering the strain in the hoop direction, the following transcendental equation is determined.

$$\overline{\theta} = (\sin \bar{\theta} + \bar{R} \, \bar{C}_p / E_{cc}) \, \bar{D}_o / \bar{\ell} \tag{42}$$

where D_o is gore width of the unstretched membrane. A derivation of this equation and an iterative type solution is presented in Appendix A.

The necessary equations have now been derived to solve for the inflated shape, provided the boundary conditions are specified. For this type of structure with axisymmetric loads, it is required that the angle ϕ at the apex be zero. At the other boundary there is usually a structure that limits the deflection and also provides a means

of transferring loads. For example, a parachute would have suspension lines to transfer loads to the payload and also restrict the opening. A constraint condition, such as suspension line might provide, could be written in the form

$$\psi = \bar{R}_f + \bar{L}_s \left(1 + \bar{T}/\bar{E}_s\right) \cos \phi_f = 0 \tag{43}$$

where

$$\bar{E}_s = E_s/C_{p_1} \, Q \sin \pi/N \, S_L \tag{44}$$

All other boundary conditions are known, or can readily be determined, with the exception of $\bar{T}_o$ for which the magnitude is determined by iterating on the constraint condition ψ.

2. SOLUTIONS OF EQUATIONS FOR POLYGONAL SHAPES

Implementation of a solution to the governing equations was effected by use of a computer employing numerical methods. In effect, the problem involves the solution to four differential equations subject to two point boundary conditions. Also, for a given gore shape $D_o(S)$, a transcendental equation has to be solved for the variable $\bar{\theta}$ during each integration step. The resulting solution is the calculated shape of the deployed parachute that satisfies the structural equilibrium equations, compatibility conditions, and boundary conditions. In summary, the solution for a given polygonal shape involves solving the differential equations

$$d\phi/d\bar{S} = 2\bar{R} \sin (\bar{\theta} - \beta) \bar{S}_{TR} \bar{C}_p/T \sin \theta \tag{45}$$

$$d\bar{R}/d\bar{S} = \cos \phi \, \bar{S}_{TR} \tag{46}$$

$$d\bar{Z}/d\bar{S} = \sin \phi \, \bar{S}_{TR} \tag{47}$$

$$d\bar{T}/d\bar{S} = 2\bar{R} \sin \pi/N \cos \phi \cos (\bar{\theta} - \beta) \bar{S}_{TR} \bar{C}_p/\sin \bar{\theta} \cos \beta \tag{48}$$

where

$$\beta = \sin^{-1} (\sin \pi/N \sin \phi) \tag{49}$$

and the transcendental equation

$$\bar{\theta} = (\sin \bar{\theta} + \bar{R}\, \bar{C}_p/\bar{E}_{cc})\, \bar{D}_o/\bar{\ell} \tag{50}$$

with the initial conditions

$$\bar{S} = \bar{S}_o$$

$$\bar{R} = \bar{R}_o$$

$$\phi = \pi/2$$

$$\bar{Z} = 0$$

$$\bar{T} = ?$$

Boundary condition constraint requires that $\bar{T}_o$ be selected so that

$$\psi = \bar{R}_f + \bar{L}_s\, (1 + \bar{T}_f/\bar{E}_s) \cos \phi_f = 0 \tag{51}$$

The initial conditions for $\bar{R}_o$ and $\bar{Z}_o$, $\bar{S}_o$, are known from geometric conditions.

These equations can be compared with other references by letting some of the parameters take extreme values. For example, the Taylor shape is found by applying Taylor's original assumptions; that is,

the number of gores are infinite

$$N \to \infty \tag{52}$$

which requires that

$$\beta \to 0 \tag{53}$$

and from equation (49) we get

$$\bar{T} = \text{constant}$$

If equations (45) and (46) are combined, the Taylor curve is obtained

$$\bar{R}^2 = C \sin \phi \tag{54}$$

It should be noted that an approximation of the Taylor curve is found if the angle $\bar{\theta}$ is selected to be

$$\bar{\theta} = \pi/2 + \beta \tag{55}$$

In reference 34, this angle was given as $\pi/2$ since the angle β was not included in the derivation. It should be noted that Taylor had determined $\bar{\theta}$ to be a constant value for a given radius regardless of

the number of gores.

Another interesting problem arises when the angle is selected such that

$$\bar{\theta} = \beta \tag{56}$$

From equation (45) we see that the angle ϕ is constant, and thus, the shape is a conical.

$$\frac{d\phi}{dS} = 0$$

From equation (48)

$$d\bar{T}/d\bar{S} = 2\bar{R} \sin \pi/N \cos \phi \, S_{TR} \, \bar{C}_p/(1/2 \sin 2\beta) \tag{57}$$

If the number of gores is sufficiently large so that

$$\sin \pi/N \approx \pi/N$$

then it is evident that

$$\sin \beta = \beta$$

and we get

$$d\bar{T} = 2\bar{R}\,\bar{C}_p\,d\bar{R}/\sin\phi \tag{58}$$

which is the meridional stress resultant of a cone. The width of the membrane needed to span the distance between chords is determined from equation (49)

$$D_o = \ell\bar{\theta}/(\sin\bar{\theta} + \bar{R}\,\bar{C}_p/\bar{E}_{cc}) \tag{59}$$

2.1 Solution for Given Gore Shapes

For a given gore shape $D_o(S)$, a particular value of the initial force in the meridional member is found such that the terminal constraint condition is satisfied. In order to satisfy this constraint, it is necessary to iterate on the initial value of the force in the meridional member. This is accomplished by first assuming a value for $\bar{T}_o$, integrating the differential equation to the terminal boundary, and then evaluating the constraint equation. An improved initial value is found that tends to reduce the error to zero.

Two methods are used to determine $\bar{T}_o$. The gradient method has been used successfully, that is

$$\bar{T}_{o_{n+1}} = \bar{T}_{o_n} - K\left(\frac{\partial\psi}{\partial\bar{T}_o}\right)_n \tag{60}$$

where the partial derivative is determined by numerically differencing successive cycles. Note, this requires two cycles through the whole integration process to get started and must remain within the linear

region of the solution. Therefore, the initial guess of T_o, the first increment $\Delta\bar{T}$ and the constant K have to be judiciously selected; but once in the linear region of the solution, convergence is very rapid. An alternate method makes use of the relationship arrived at by considering the physical aspects of the problem; that is, when ψ is increasing, then $\bar{T}_o$ should be reduced.

$$\bar{T}_{o_{n+1}} = T_{o_n} (1 - K\psi)^2 \tag{61}$$

This later method has the advantage of starting the first step without having to guess the increment ΔT. A flow diagram showing the solution algorithm is shown in figure 6.

For the optimization process developed in a subsequent chapter, the angle $\bar{\theta}$ is determined using known techniques for finding the control variable to maximize a function. Once $\bar{\theta}$ is known, the gore geometry $D_o(S)$ is found from the geometric relationship relating θ to $\bar{R}$.

2.2 Analysis of Existing Parachute Input Data

2.2.1 Material Properties and Pressure Coefficients

The required input data for a solution to these equations involves the gore geometry, material stiffness, suspension line length, and the applied pressure. These data could be supplied in nondimensional form, but in order to compare results with existing designs, the following input was used as a baseline reference (ref. 31)

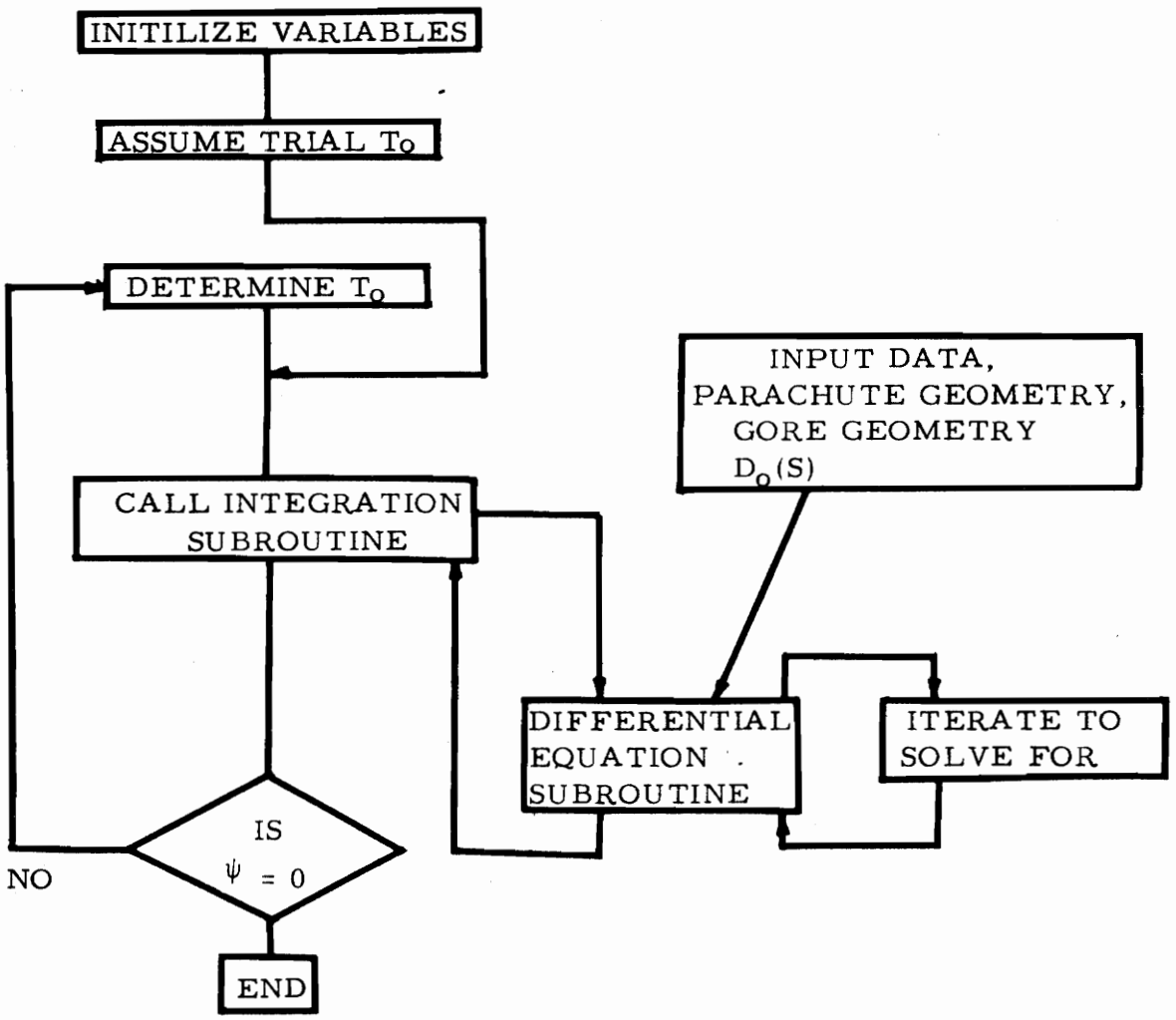

Figure 6.- Parachute program flow diagram.

$$S_L = 14 \text{ ft}$$

$$Q = 14 \text{ lbs/ft}^2$$

$$E_{cc} = 2000 \text{ lb/ft}$$

$$E_{RT} = 2000 \text{ lb}$$

$$N = 28$$

where S_L is the maximum constructed radius, Q is the equilibrium dynamic pressure, N is the number of gores, E_{cc} and E_{RT} the stiffness of the canopy cloth, and the radial tape, respectively.

The early investigators dealing with parachute designs considered only constant pressure distributions. There is ample test data available indicating that the pressure increases near the outer skirt; however, much preliminary design effort is still based on the assumption that the pressure is constant. Two coordinate systems are usually used to display pressure variations: they are pressure coefficient plotted versus either the angle ϕ or the distance S.

Since the independent variable to be used later in the optimization section is the angle $\bar{\phi}$, it was decided to express C_p as a function of $\bar{\phi}$ and use throughout this study in order to make fair comparisons of the different designs. Shown in figure 8 as a solid line is a plot of the polynomial expression representing the pressure distribution. Also shown in this figure is the data taken from references 16 and 31. The same polynomial expression plotted as a

function of $\bar{S}$ is shown in figure 7. When noting the scatter in test data from these plots, it was felt that the polynomial curve represents a rather general pressure distribution of several parachutes of diverse geometry.

The following expression was used for the pressure coefficient:

$$C_p = 1.3 + .52\bar{\phi} - .25\bar{\phi}^2 + .4\bar{\phi}^3 \tag{62}$$

This expression is normalized so that only the distribution enters into the equations. The normalization factor has been included in the nondimensionalized expression for the reference force T_R.

It should be mentioned that the opening shock loads can be evaluated with the methods presented in this study, provided the appropriate pressure coefficients are used, and the meridional membrane stress is neglected (refs. 13 and 18).

The typical type of fabric used in parachute design is orthotropic, and since the loading is usually in the bias direction, a transformation of the material properties is required. Given the material constitutive relationships in one coordinate system, the properties in a rotated system are determined from the relationship (ref. 7)

$$\{\sigma\}_{ROT} = [T]^{-1} [Q] [T] \{\varepsilon\}_{ROT} \tag{63}$$

where the transformation matrix is defined

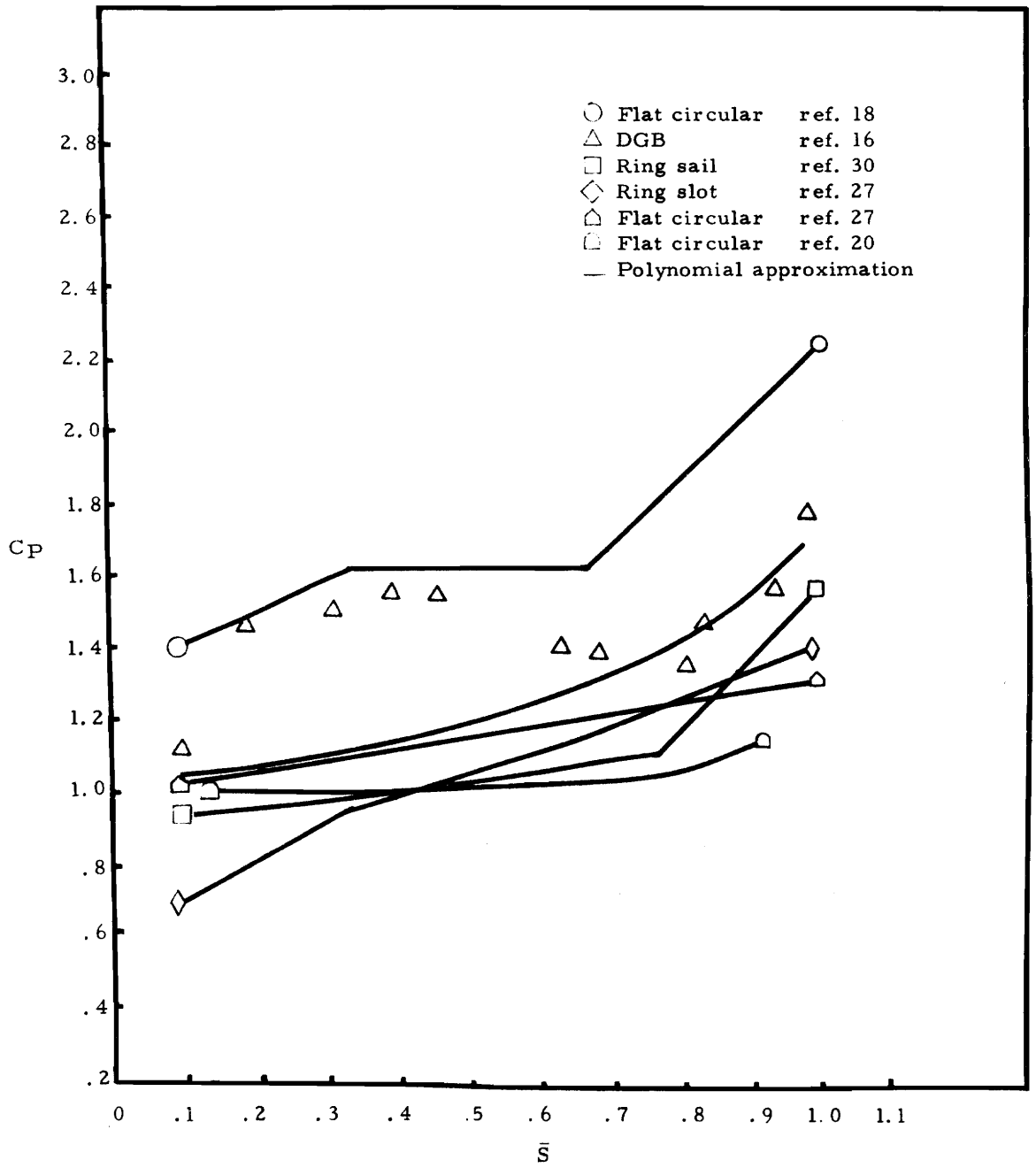

Figure 7.- Pressure distribution.

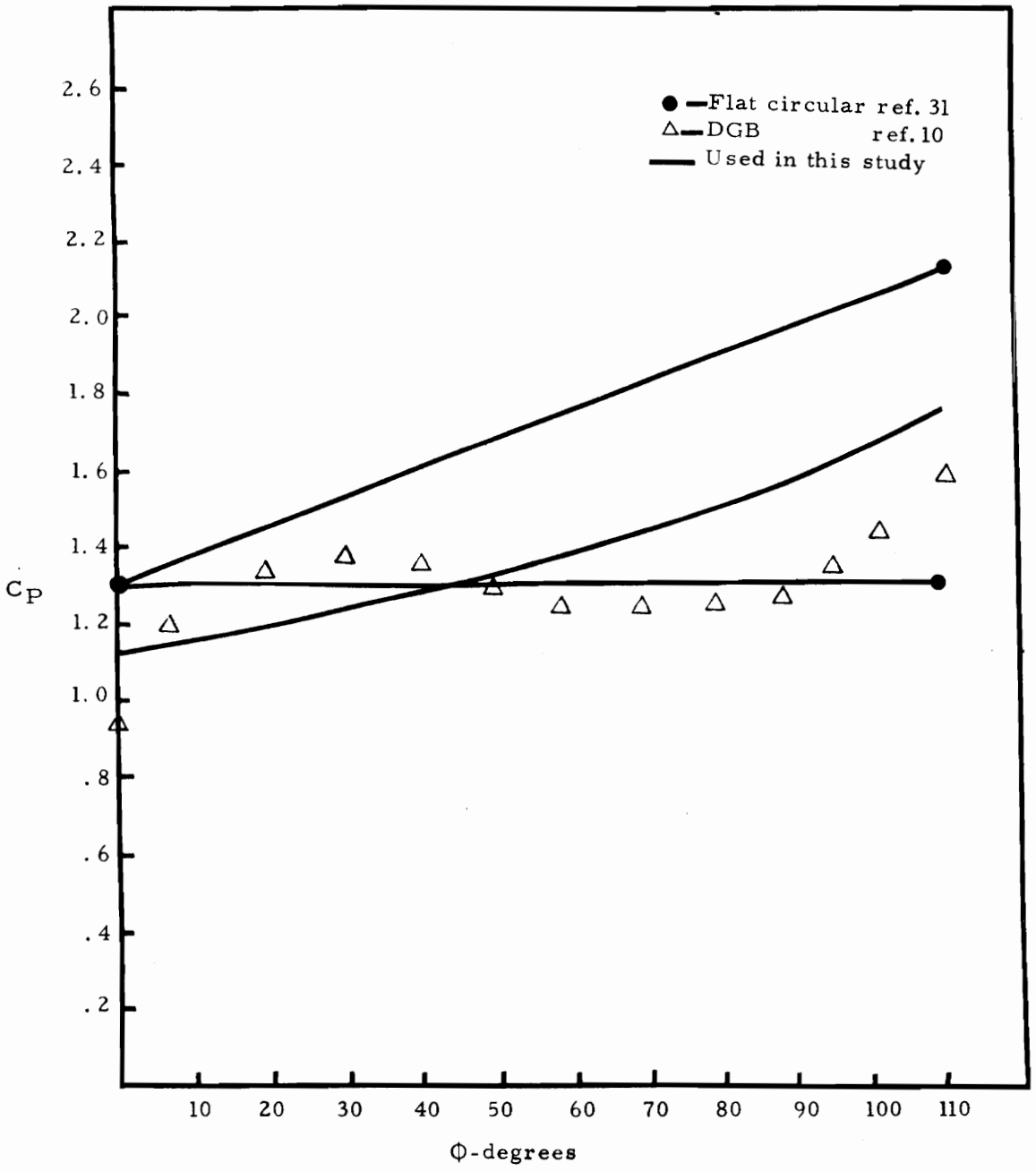

Figure 8.- Pressure distribution.

$$[T] = \begin{bmatrix} m^2 & n^2 & 2mn \\ n^2 & m^2 & -2mn \\ -mn & -mn & m^2-n^2 \end{bmatrix}$$

and the original constitutive matrix is

$$[C] = \begin{bmatrix} C_{11} & C_{12} & 0 \\ C_{21} & C_{22} & 0 \\ 0 & 0 & C_{33} \end{bmatrix}$$

Elements of the matrices are

$$m = \cos \alpha$$

$$n = \sin \alpha$$

$$C_{11} = E_{\theta\theta}/(1 - \nu_{\theta\phi}\nu_{\phi\theta}) \tag{64}$$

$$C_{22} = E_{\phi\phi}/(1 - \nu_{\theta\phi}\nu_{\phi\theta})$$

$$C_{12} = \nu_{\theta\phi}E_{\theta\theta}/(1 - \nu_{\theta\phi}\nu_{\phi\theta}) = \nu_{\phi\theta}E_{\phi\phi}/(1 - \nu_{\theta\phi}\nu_{\phi\theta})$$

$$C_{33} = G$$

and α is the angle of rotation.

2.2.2 Geometry of Existing Parachutes

A baseline for evaluating the optimized structure is established by analyzing existing designs. Several of the more conventional designs are analyzed to establish performance indices, load distribution, and deployed shapes. The dimensions of the gore shape needed for solving equations (45) - (48) are given below. A comparison of the results with other references and test data are made and indicate that the governing equations produce adequate correlation.

First to be considered is the solid flat circular parachute. This parachute has seen much service and has the most data on structural loads (references 3, 19, and 31). Shown below is the constructed shape of this parachute.

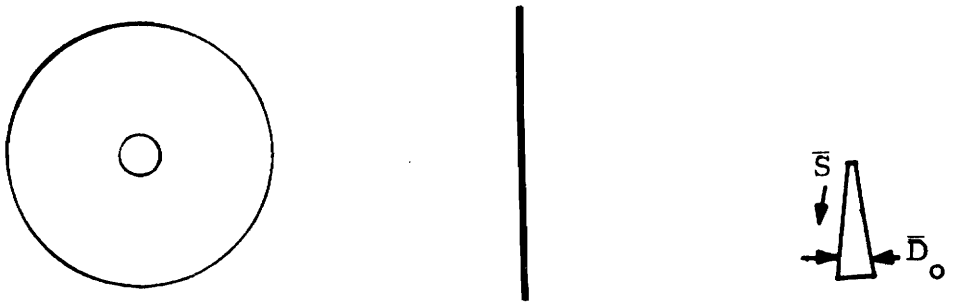

Figure 9.- Flat circular parachute.

The equation for the gore geometry is

$$\bar{D}_o = (\bar{S} + .025)\ \pi/N \tag{65}$$

where the radial tapes are 2.5 percent shorter than the gore radial distance (ref. 3).

A similar parachute to flat circular is the extended skirt. Shown in figure 10 is the constructed shape.

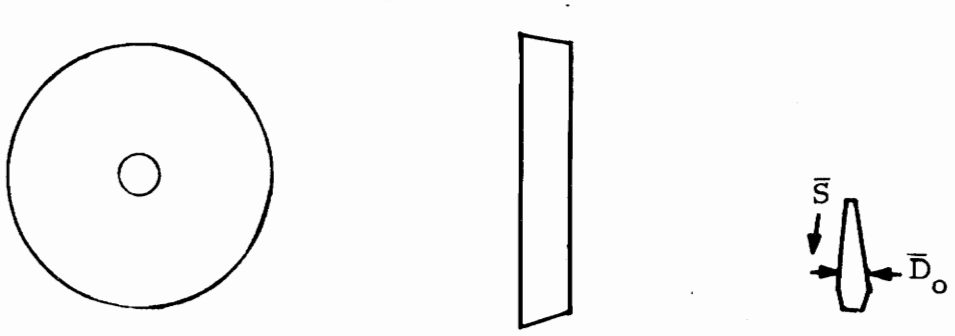

Figure 10.- Extended skirt parachute.

The expression for this gore shape is

$$\bar{D}_o = 2\pi/N\ (\bar{S} + .025) \qquad \bar{S} < .85$$

$$= 2\ (.875\ \pi/N - 12.75\ (\bar{S} - .085)) \qquad \bar{S} \geq .85 \tag{66}$$

Another parachute that is frequently used is the conical parachute. Its geometry is shown in figure 11

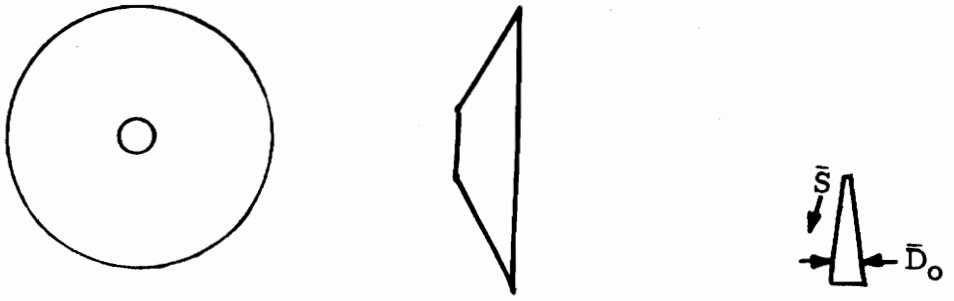

Figure 11.- Conical parachute.

and the equation for the gore is

$$\bar{D}_o = 2\xi \sin^{-1} (\sin 20^\circ \sin \pi/N) \tag{67}$$

A fourth parachute to be compared is the 1/4 spherical parachute. The constructed shape is actually generated from the spherical coordinates of a spherical surface. The geometry is shown in figure 12.

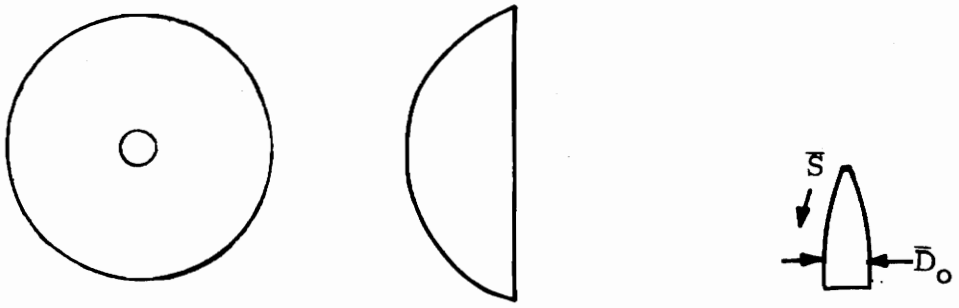

Figure 12.- 1/4 Spherical parachute.

The gore is computed from the equations

$$\bar{D}_o = R_1 \pi \sin S/N \tag{68}$$

where R_1 is defined as (ref. 4)

$$R_1 = 1$$

2.2.3 Results and Discussion

The parachutes presented in the previous section were analyzed to provide a basis for evaluating the optimum design. Since test data were available on measured hoop stresses and inflated profile shapes, a comparison was made to evaluate the accuracy of the analytical results. Drag coefficients were calculated to determine the merits of the various gore shapes and to later be used for evaluating the optimized design.

The deployed shape of a Disk-Gap-Band parachute (ref. 16) is shown in figure 13. Included in this figure are the constructed and measured shapes. The constructed shape is defined as the actual fabricated geometric shape.

Figure 14 shows the hoop stress distribution for a flat circular type parachute. From this figure, the high stress area in the crown region is evident. Also, note the low magnitude of the stresses; the nondimensional stress is defined as

$$\bar{N}_\theta = N_\theta S_L / T_R \tag{69}$$

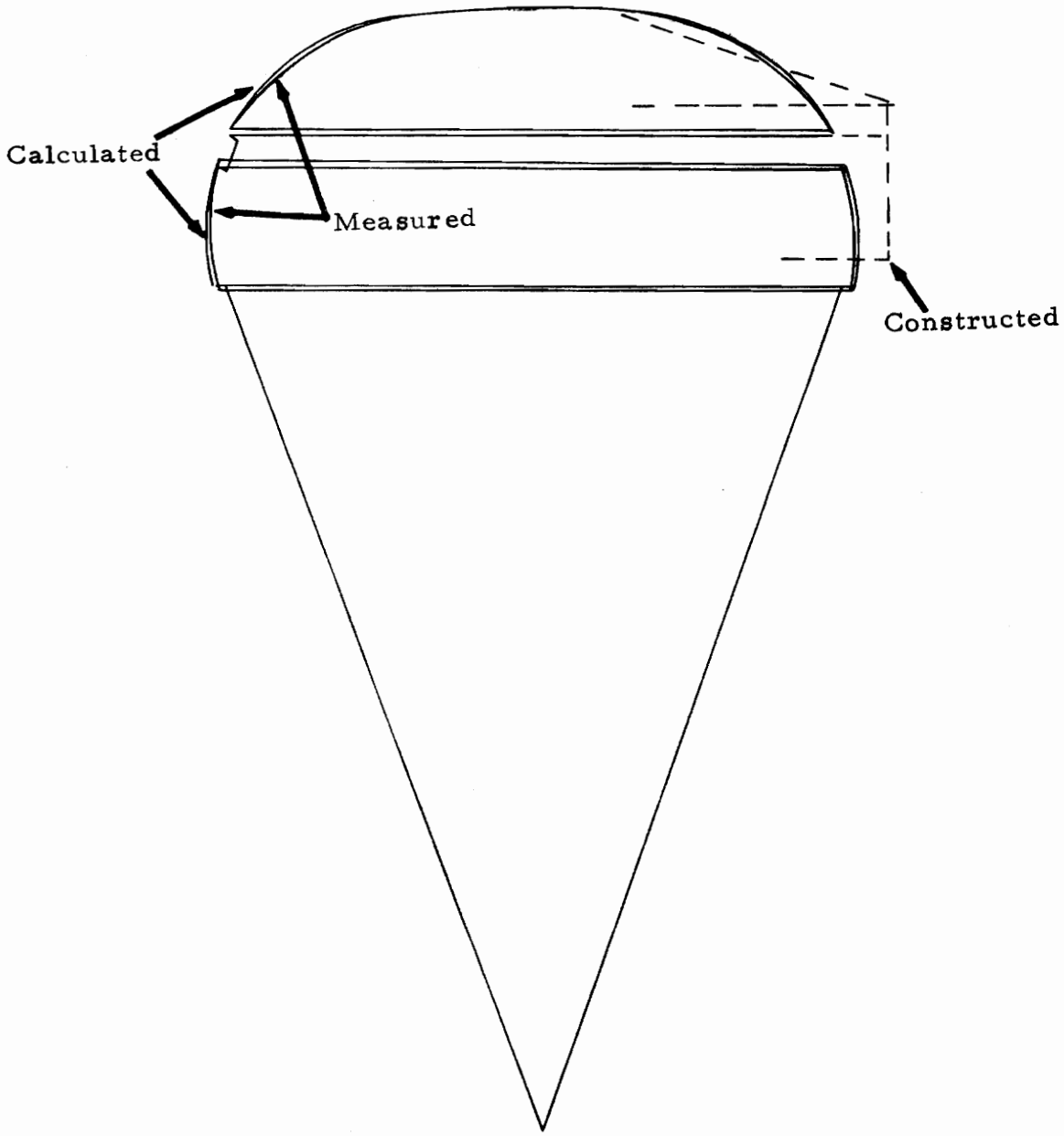

Figure 13.- Comparison of constructed, calculated, and measured canopy profile, ref. 16.

Also shown in this plot is the stress distribution taken from reference 31.

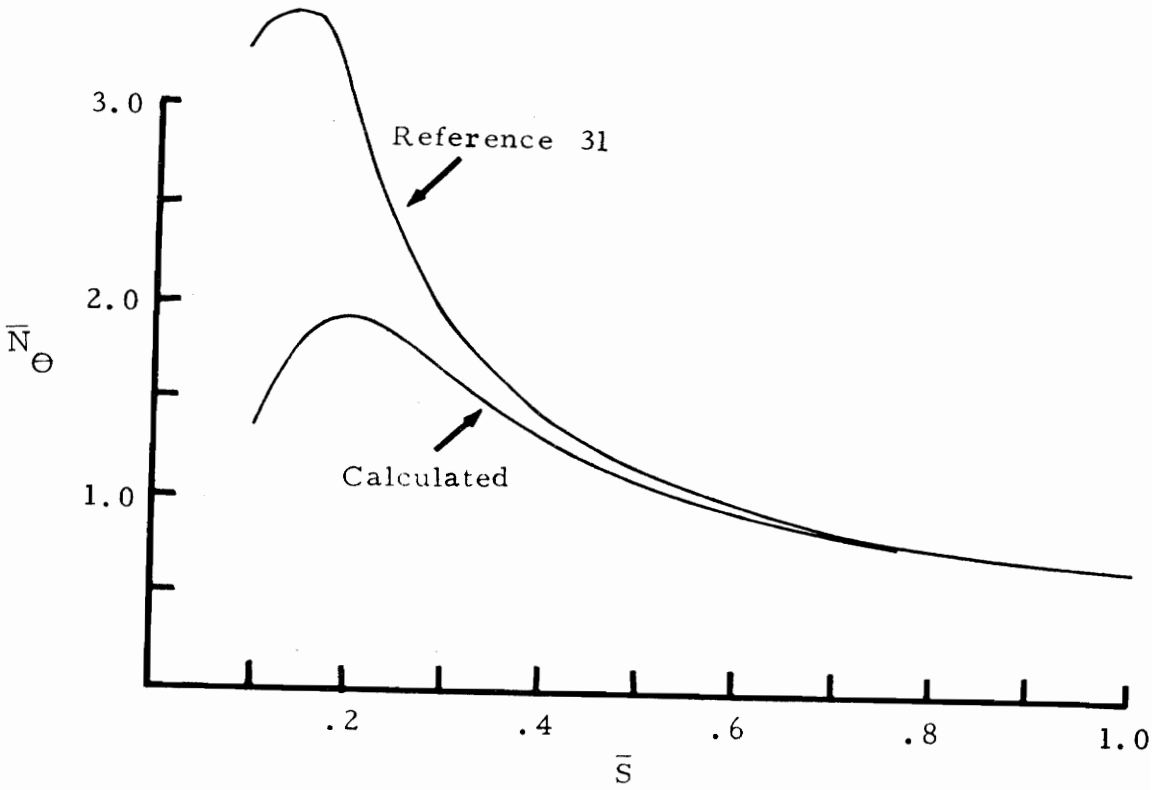

Figure 14. - Comparison of calculated membrane stress with reference 31

When comparing these results it should be noted that the method used in the reference has neglected the angle β. This in effect decreases the lobing angle in the critical region near the vent, whereas, near the skirt it becomes less important since the lobing angle is large. Thus there are large differences in the vent region; however, good agreement was obtained near the skirt.

Parachute canopy stresses were measured experimentally by Heinrich and the results reported in reference 20. In this experiment, a two-foot-diameter parachute was tested in a wind tunnel with a special type strain gage attached to the fabric for taking measurements. During the test it was found that the test model was not truly a flat circular parachute, but assumed a conical form. The corresponding stresses were adjusted to account for this deviation.

Calculated stresses from the program presented in this thesis are compared with the test data. Since the test article was not truly a flat circular parachute, the results of a 20° conical parachute are also shown.

TABLE 1

Comparison of Calculated and Measured Parachute Membrane Stresses

Meridional distance	Measured stress $\bar{N}_\theta$	$\bar{N}_\theta$ Calculated for flat circular	$\bar{N}_\theta$ Calculated for conical
$\bar{S} = .5$	2.04	1.36	2.78
$\bar{S} = .75$	1.49	1.03	1.14
$\bar{S} = .95$	.77	.92	.93

Of interest is the comparison of the coefficient of drag for the parachutes studied in the previous section. Shown in figure 15 is a plot of the relative merit.

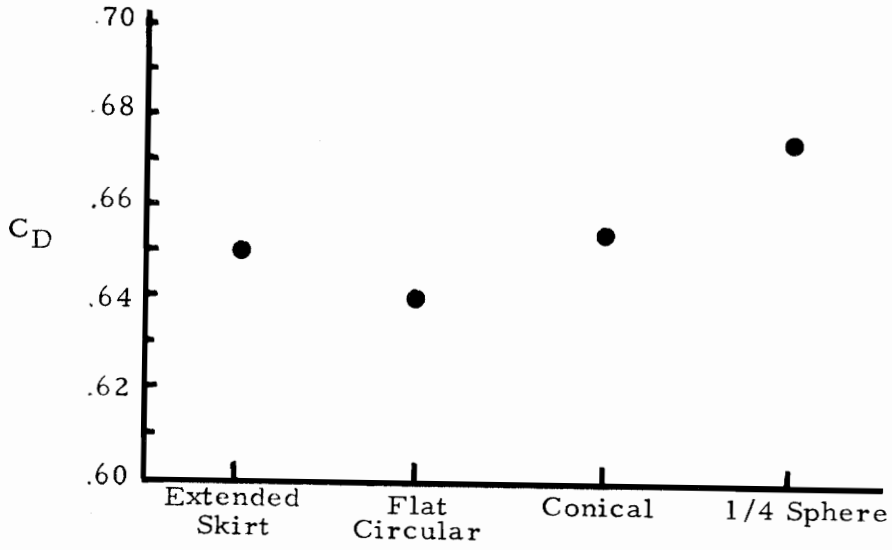

Figure 15.- Comparison parachute drag coefficient.

From the analysis of existing parachutes, we see the effect on drag coefficients for various gore dimensions. It will be shown in a later section that an optimum design closely resembles the 1/4 sphere.

Drag coefficients vary from .640 for the flat circular to a maximum of .681 for conical parachute. It should be noted that the conical design would not be superior if the hoop stress levels were required to be comparable to the 1/4 sphere. The conical parachute lobing is very small, $\bar{\theta}$ is about 3° in the critical region near the vent. Resulting stresses are at least 6 times greater than the other designs. In comparing the drag coefficient, consideration should be given to the minimum allowable lobing.

The computer program developed in this section was one of the analytical tools used in analyzing the failure of the Viking Project BLDT-1 parachute, see reference 1. Also used in this investigation was the Apollo parachute computer program (ref. 30). The two methods provided a means of verifying the failure mode.

When comparing the results of the calculated membrane stresses using the two methods, there were differences in the region near the vent as well as the mid radius; nevertheless, good agreement was obtained in the outer region near the skirt. In the vent area, (ref. 30) calculated stresses are lower but become higher near the mid radius. Assessing the variations of the two methods, it is believed that the primary cause of the difference is due to the vent boundary condition. As mentioned in the Mullin's report, the angle ϕ_o does not have to be zero at the apex. In all other respects, the two methods are similar with only the technique for solving the differential equations being different.

An interesting technique is shown in the BLDT-1 failure report (ref. 1) for determining a particular pressure distribution that satisfies the failure conditions. Three conditions were known at failure: the total drag load, the maximum deployed radius, and the load capability of the fabric at failure. These were imposed as constraints for determining the coefficients of a polynomial representing the pressure distribution. A solution was obtained by use of a Newton-Raphson iteration technique. The derived pressure curve peaked in an area where the failure was initiated.

Some of the salient features found by analyzing these parachutes are enumerated below.

The effect of various gore shapes was shown by analysis to significantly influence the drag coefficient; also, the sensitivity due to changes in geometry can be seen by comparing the drag of the different designs. The parachute producing the maximum drag coefficient is the conical, whereas, the maximum drag force results from a flat circular parachute. Effects of varying the geometry of the gore have shown variations in the drag coefficient from .640 to .681.

The calculated drag coefficients are consistently low when compared to test data (ref. 3). This is believed to be caused by not including factors such as, gliding, oscillatory motion, and skin friction.

Pressure distributions appear to be relatively insensitive to various geometric shapes, and therefore is approximated by a general distribution.

The membrane hoop stress peaks in the region near the vent, an area that is critical during opening. Numerous design techniques are used to arrive at desired stresses. Such things as, shortening of the tapes in the crown regions, omitting gores and adding gore fullness have been used.

In order to judge the merits of each parachute fairly, the geometry input was the same whenever possible. For example, the suspension lines in each case were twice as long as the canopy radius,

the tapes were shortened 2-1/2 percent of the constructed radius, and the pressure distribution was the same. In actual parachute application there are many variations of these conditions; however, this study is confined to assessing variations of gore shapes only.

3. OPTIMIZATION EQUATIONS

In this section, the necessary conditions are developed which provide the design of parachute gore shapes for optimal drag performance.

The influence of gore shapes on the drag performance for several current designs was presented in the previous section. A general law controlling the gore shape is needed to insure an optimum design.

The problem is formulated so as to be able to utilize the well established mathematical theory for determining optimal processes. Several methods are used to obtain solutions: the first being an application of the maximum principle, and the second scheme involves two numerical techniques. The numerical solutions employed the steepest descent and the Rayleigh-Ritz methods.

Numerous parameters are to be considered when selecting the geometric shape of a polygonal type of structure. Such factors as opening characteristics, dynamic stability, opening peak stresses, weight or bulk are among many design considerations. Of primary importance is the steady-state drag performance of the decelerator. The objective functions to be optimized in this research are the drag characteristics. Two cases will be investigated: first involves the minimization of the total drag and the second maximizes the drag coefficient. The control variable to be selected in the optimization process is the angle $\bar{\theta}$. Once this angle is a known function of the independent variable $\bar{S}$, then the shape of the gore is determined from the known geometry. Constraints are imposed on the

control variable and are determined by maximum stress conditions when $\bar{\theta}$ is small, and stability limitations when $\bar{\theta}$ is large.

The two performance indices investigated are the maximum drag force

$$\Phi = -\bar{T}_f \sin \phi_f$$

where the subscript f stands for the conditions at $\phi = \phi_f$ and the drag coefficient

$$\Phi = -\bar{T}_f \sin \phi_f / \bar{A}_f \tag{71}$$

where $\bar{A}$ is the area of the gore and the subscript f designates quantity at the final point. Conversion to the more common terminology is found by multiplying equation (71) by $C_p \sin \pi/N$ to get

$$C_D = C_{p_1} \sin \pi/N \, \Phi \tag{72}$$

An additional equation for the state variable $\bar{A}$ is required for the drag coefficient objective function. Using the expression for D_o, equation (59), and the dimension dS, equation (17), results in

$$dA/dS = 2R \sin \pi/N \, \bar{\theta}/\sin \bar{\theta}/\sin \bar{\theta} \, (1 + C_p \, Q \sin \pi/N \, R/\sin \bar{\theta} \, E_{cc}) \tag{73}$$

Nondimensionalizing gives

$$\frac{d\bar{A}}{d\bar{S}} = 2\bar{R} \sin \pi/N \; \bar{\theta}/\sin \bar{\theta} \; (1 + \bar{C}_p \; \bar{R}/\sin \bar{\theta} \; \bar{E}_{cc}) \tag{74}$$

3.1 Necessary Conditions

The problem of interest is to maximize the value of a performance index $\Phi(x_f, t_f)$ for a system which is governed by the equations

$$\dot{x} = f(x, u, t) \tag{75}$$

where x is a vector of state variables, and u is a vector of control variables, which may also have initial and terminal constraints on the state variables $\psi(x, t)_o, \psi(x, t)_f$ and possibly constraints on the control variable u.

The necessary conditions for a solution $u(t)$ for this problem are given below.

Define

$$H = \lambda^T(x, \lambda, t) \; f(x, u, t) \text{ (Hamiltonian)} \tag{76}$$

where the variables λ are determined from

$$\dot{\lambda} = - \frac{\partial H}{\partial x} \tag{77}$$

Then the necessary conditions for an optimal control $u(t)$ are

1. H must be a maximum with respect to u which for the case when u is not on its boundary can be expressed as $\frac{\partial H}{\partial u} = 0$.
2. $d\Phi + \mu_i \, d\psi_i - Hdt + \lambda^T dx = 0$ evaluated at its initial and final conditions.
3. λ vector be non zero. (78)

For the problem of interest

$$\Phi = -\bar{T}_f \sin \phi_f \qquad \text{or} \qquad \Phi = -\bar{T}_f \sin \phi_f / \bar{A}_f \tag{79}$$

$$x^T = (S \; R \; Z \; T \; A \; \phi)$$

$$u = \bar{\theta} \qquad\qquad \bar{\theta}_{min} \leq \theta \leq \bar{\theta}_{max}$$

and the independent variable selected to be ϕ. The reason for the change of independent variable is that it offers several advantages such as, simplification of the $d\bar{T}/d\phi$ equation, and the elimination of the terminal constraint condition. The state equations with the independent variable ϕ become

$$d\bar{S}/d\phi = \bar{T} \sin \phi / (2 \bar{C}_p \bar{R} \sin (\bar{\theta} - \beta) S_{TR}) \tag{80}$$

$$d\bar{R}/d\phi = \cos \phi \sin \bar{\theta} \, \bar{T} / (2 \bar{C}_p \bar{R} \sin (\bar{\theta} - \beta) \tag{81}$$

$$d\bar{Z}/d\phi = \sin \phi \sin \bar{\theta}\, \bar{T}/(2\, \bar{C}_p\, \bar{R} \sin (\bar{\theta} - \beta)) \tag{82}$$

$$d\bar{T}/d\phi = \sin \pi/N \cos \phi\, \bar{T}/(\cos \beta \tan (\bar{\theta} - \beta)) \tag{83}$$

$$d\bar{A}/d\phi = \sin \pi/N\, \bar{T}\, \bar{\theta}/(\sin (\bar{\theta} - \beta)\, \bar{C}_p\, S_{TR}\, (1 + \bar{C}_p\, \bar{R}/\bar{E}_{cc} \sin \bar{\theta}) \tag{84}$$

where the initial and terminal conditions are given by

$$\begin{aligned} \bar{T}(\phi_o) &= \bar{T}_o \\ \bar{S}(\phi_o) &= \bar{S}_o \\ \bar{R}(\phi_o) &= \bar{R}_o \\ \bar{Z}(\phi_o) &= 0 \\ \bar{A}(\phi_o) &= 0 \\ \phi_o &= 0 \end{aligned} \tag{85}$$

and

$$\begin{aligned} &\bar{T}(\phi_f) \text{ unspecified} \\ &\bar{S}(\phi_f) \text{ unspecified} \\ &\bar{R}(\phi_f) \text{ unspecified} \\ &\bar{Z}(\phi_f) \text{ unspecified} \\ &\bar{A}(\phi_f) \text{ unspecified} \\ &\phi_f \quad \text{given} \end{aligned} \tag{86}$$

The transversality conditions (equation 78) yield the following conditions at the initial and terminal point.

$$\begin{aligned} &\text{initial point,} && \text{- no additional information} \\ &\text{final point} && -\lambda_{S_f} = \lambda_{Z_f} = \lambda_{R_f} = 0 \end{aligned} \tag{87}$$

and

$$\lambda_{T_f} = \sin \phi_f;\ \lambda_{A_f} = 0 \tag{88}$$

for the first case and

$$\lambda_{T_f} = \sin \phi_f / \bar{A};\ \lambda_{A_f} = -\bar{T} \sin \phi_f / \bar{A}^2 \tag{89}$$

for the second case.

The Hamiltonian becomes

$$H = \lambda_S(-\bar{T} \sin \bar{\theta}/(2\ \bar{C}_p\ R \sin\ (\bar{\theta} - \beta)\ \bar{S}_{TR}$$

$$+ \lambda_R(-\cos\ \phi \sin\ \bar{\theta}\ T/(2\ \bar{C}_p\ \bar{R} \sin(\bar{\theta} - \bar{\beta})$$

$$+ \lambda_Z(-\sin\ \phi \sin\ \bar{\theta}\ \bar{T}/(2\ \bar{C}_p\ \bar{R} \sin(\bar{\theta} - \beta)$$

$$+ \lambda_T(-\sin\ \pi/N \cos\ \phi\ \bar{T}/(\cos\ \beta \tan(\bar{\theta} - \beta)$$

$$+ \lambda_A(-\sin\ \pi/N\ \bar{T}\ \bar{\theta}/(\bar{C}_p \sin(\bar{\theta} - \beta)(1 + \bar{C}_p\ \bar{R}/E_{cc} \sin\ \bar{\theta})) \qquad (90)$$

and the adjoint differential equations are

$$\dot{\lambda}_S = 0$$

$$\dot{\lambda}_R = -[-T \sin\ \bar{\theta}/(2\ \bar{C}_p\ \bar{R}^2 \sin(\bar{\theta} - \beta)S_{TRT}\ \lambda_S - T \cos\ \phi \sin\ \bar{\theta}/(2\ \bar{C}_p\ \bar{R}^2 \sin(\bar{\theta}-\beta)\lambda_R$$

$$-\sin\ \phi \sin\ \bar{\theta}\ \bar{T}/(2\ \bar{C}_p\ \bar{R}^2 \sin\ (\bar{\theta} - \beta)\lambda_T - \bar{T}\ \bar{\theta} \sin\ \pi/N\ \bar{C}_p/(\sin(\bar{\theta} - \beta)$$

$$\bar{E}_{cc} \sin\ \bar{\theta}(1 + \bar{C}_p\ R/\bar{E}_{cc} \sin\ \bar{\theta}))\lambda_A]$$

$$\dot{\lambda}_Z = 0$$

$$\dot{\lambda}_T = -[\sin \bar{\theta}/(2\ \bar{C}_p\ \bar{R}\ \sin(\bar{\theta} - \beta)S_{TR}^2)\lambda_S + \cos \phi \sin \bar{\theta}/(2\ \bar{C}_p\ \bar{R}\ \sin(\bar{\theta} - \beta)\lambda_R$$

$$+ \sin \phi \sin \bar{\theta}/(2\ \bar{C}_p\ \bar{R}\ \sin(\bar{\theta} - \beta)\lambda_Z + \sin \pi/N \cos \phi/\cos \beta \tan(\bar{\theta} - \beta)\lambda_T$$

$$+ \sin \pi/N\ \bar{\theta}/(\bar{C}_p \sin(\bar{\theta} - \beta)(1 + \bar{R}\ \bar{C}_p/(\bar{E}_{cc} \sin \bar{\theta})]\lambda_A$$

$$\dot{\lambda}_A = 0 \qquad (91)$$

where for the drag only case $\lambda_A = 0$ (equation 88).

For the case where the control variable $\bar{\theta}$ is not on its boundary

$$\frac{\partial H}{\partial \theta} = \frac{\bar{T}}{2\ \bar{C}_p\ \bar{R}} (\sin(\bar{\theta} - \beta)\cos \bar{\theta} - \sin \bar{\theta} \cos(\bar{\theta} - \beta)/\sin^2(\bar{\theta} - \beta))[\lambda_S/S_{TR} +$$

$$\cos \phi\ \lambda_R + \sin \phi\ \lambda_Z] - \sin \pi/N \cos \phi\ \bar{T}/(\cos \beta \sin^2(\bar{\theta} - \beta)\lambda_T$$

$$+ \frac{\sin \pi/N\ \bar{T}}{\bar{C}_p} [1/\sin(\bar{\theta} - \beta)S_{TR}(1 + \bar{C}_p\ \bar{R}/E_{cc} \sin \bar{\theta}) - \bar{\theta} \cos(\bar{\theta} - \beta)/$$

$$(\sin^2(\bar{\theta} - \beta)S_{TR}(1 + \bar{R}\ \bar{C}_p/E_{cc} \sin \bar{\theta}) + \bar{R}\ \bar{C}_p \cos \bar{\theta}\ \bar{\theta}/\sin(\bar{\theta} - \beta)$$

$$S_{TR}(1 + \bar{C}_p\ \bar{R}/E_{cc} \sin \bar{\theta})^2\ \bar{E}_{cc} \sin^2 \bar{\theta}]\lambda_A \qquad (92)$$

When the control variable $\bar{\theta}$ is on its boundary and equation 92 can not always be satisfied, $\bar{\theta}$ is selected $\bar{\theta} = \bar{\theta}_{max}$, or $\bar{\theta} = \bar{\theta}_{min}$ so that H is as large as possible.

4. SOLUTION OF THE OPTIMIZATION EQUATIONS

Several methods were used to solve the optimization equations. The first method attempted was a direct attempt to solve the state and Euler-Lagrange equations by guessing the initial conditions for the λ's; numerically integrating the differential equations, and employing the Newton-Raphson technique to satisfy the terminal constraint conditions. When this method was unsuccessful, the steepest descent technique was attempted, but again without success. A third method similar to a Rayleigh-Ritz technique was used, and the resulting solution was thought to have converged, although no confirmation could be obtained by other methods.

The terminal boundary constraint was the source of the convergence difficulty, and it was decided to recast the problem so that an embedding technique could be used. This was made possible by the change in the independent variable from $\bar{S}$ to ϕ. Thus, the terminal constraint condition, equation (43), could be replaced with ϕ_f = constant. As a result the necessary conditions observed in equation 78 allow simplification of the Hamiltonian and eliminate the terminal boundary constraint. Consequently, it makes an analytic solution possible in the simple drag case and simplifies the numerical solutions in the drag coefficient case. In fact, no convergence problems were encountered after this change was made. The initial condition for the variable $\bar{T}$ is varied until the condition $\bar{S}_f = 1$ is satisfied. Thus a series of optimal trajectories are found with only one solution satisfying the terminal condition for $\bar{S}_f$.

4.1 Solution Using Maximum Principle

When the objective function is the drag force, the optimization conditions are greatly simplified and the optimization problem can be solved analytically. The objective function to be maximized is the drag force.

$$\Phi = -\bar{T}_f \sin \phi_f \tag{93}$$

Since this is a nonintegral performance index, the problem can be recast in the form for the application of the maximum principle by the addition of a state and control variable (ref. 25). The effect of this change is the addition of the performance index as a transversality condition at the terminal boundary. Therefore

$$\begin{Bmatrix} \lambda_S \\ \lambda_R \\ \lambda_Z \\ \lambda_T \\ \lambda_A \end{Bmatrix}_{\phi_f} = \begin{Bmatrix} 0 \\ 0 \\ 0 \\ \sin \phi_f \\ 0 \end{Bmatrix} \tag{94}$$

This problem is further reduced by the fact that the following multipliers vanish from the Hamiltonian since they are constant and are required to be zero (equation 87) at the terminal boundary; therefore

$$\begin{Bmatrix} \lambda_S \\ \lambda_Z \\ \lambda_A \end{Bmatrix} = \begin{Bmatrix} 0 \\ 0 \\ 0 \end{Bmatrix} = \text{CONSTANT} \tag{95}$$

which leaves only two adjoint variables λ_R and λ_T to enter into the solution. The equations necessary for an optimal solution have been reduced to the following

$$d\bar{T}/d\phi = \sin \pi/N \cos \phi \, \bar{T}/(\cos \beta \tan (\bar{\theta} - \beta) \tag{96}$$

$$H = \sin \pi/N \cos \phi \, \lambda_T/\cos \beta \tan(\bar{\theta} - \beta) \tag{97}$$

$$\dot{\lambda}_T = -\sin \pi/N \cos \phi \, \lambda_T/(\cos \beta \tan(\bar{\theta} - \beta) \tag{98}$$

$$\dot{\lambda}_R = \cos \phi \sin \bar{\theta} \, \bar{T}/(2 \, \bar{C}_p \, \bar{R}^2 \sin(\bar{\theta} - \beta))\lambda_R \tag{99}$$

$$\lambda_{T_f} = \sin \phi_f \tag{100}$$

The λ_R adjoint equation (equation 99) can be written

$$d\lambda_R/\lambda_R = f(\phi, \bar{\theta}, \bar{T}, \bar{R}) \, d\phi \tag{101}$$

and integrating gives

$$\lambda_R = C \, e^{\int_{\phi_o}^{\phi_f} f(\phi, \bar{\theta}, \bar{T}, \bar{R}) \, d\phi}$$

where the function is defined as

$$f = \cos\phi \sin\bar{\theta}\, \bar{T}/(2\, \bar{C}_p\, \bar{R}^2 \sin(\bar{\theta} - \beta)) \tag{102}$$

For λ_R to be zero at ϕ_f then either

$$C = 0$$

or

$$\int_{\phi_o}^{\phi_f} f(\phi, \bar{\theta}, \bar{T}, \bar{R})\, d\phi = -\infty$$

Upon examining the terms in this function, it can be shown that

$$|f(\phi, \bar{\theta}, \bar{T}, \bar{R}| << \infty$$

and therefore the integral has a finite limit which requires that C be zero.

Consequently

$$\lambda_R = \text{CONSTANT} = 0 \tag{103}$$

Integrating equation (98) gives

$$\lambda_T = C\, e^{\int_{\phi_o}^{\phi_f} \sin \pi/N \cos\phi/\cos\beta \tan(\bar{\theta} - \beta) d\phi} \tag{104}$$

and from the expression for the angle β (equation 49) when taking the derivative, we get

$$d\beta = \sin \pi/N \cos \phi \, d\phi/\cos \beta \tag{105}$$

which allows equation (104) to be simplified by a change in the independent variable. Substituting equation (105 into 104) and integrating gives

$$\lambda_T = -c \sin(\bar{\theta} - \beta) \quad \text{for} \quad \phi < \pi/2$$

and changes sign when $\phi > \pi/2$. Applying the boundary condition given by equation (100), we get

$$\lambda_T = \sin \phi_f \sin(\bar{\theta}_{max} - \beta)/\sin(\bar{\theta}_{max} - \sin \pi/N \sin \phi_f) \tag{106}$$

At $\phi = \pi/2$, the Hamiltonian changes sign due to the cosine term; however, λ_T keeps the same sign. For the Hamiltonian to be a maximum, then

$$\bar{\theta} = \bar{\theta}_{max}$$

for $\pi/2 < \phi < \phi_f$ since H is negative, and switches to $\bar{\theta}_{min}$ for $\phi < \pi/2$ since the Hamiltonian is positive. When $\phi = \pi/2$ then

$$\frac{\partial H}{\partial \bar{\theta}} = 0$$

regardless of what the value of $\bar{\theta}$ is due to the presence of the cosine term. Investigation of the following derivative

$$\frac{d}{d\phi}\left(\frac{\partial H}{\partial \bar{\theta}}\right) \neq 0 \tag{107}$$

shows that a singular condition cannot exist for a finite change in ϕ.

An interesting result is obtained if $\bar{\theta}$ is allowed to become equal to β, then equation (107) could be zero provided ϕ remains constant. Equation (107) is satisfied by the expression

$$\tan(\bar{\theta} - \beta) = \cos \phi \sin \pi/N / \cos \pi/N \tag{108}$$

This, however, is a trivial case since the object is to optimize the drag, and the addition of a cylindrical section in the center of a parachute would add nothing to the problem. It should be noted that $\bar{\theta}_{min}$ was selected to be 10 degrees for this research (ref. 4) and β_{max} is 6.4 degrees; therefore, equation 108 cannot be satisfied.

4.1.1 Solution of State Equations

In this section, the state differential equations $\bar{R}$ and $\bar{T}$ are solved in closed form. This is implemented by again changing the independent variable to β. A comparison will be made in a later section of the closed form solutions with those obtained by numerical methods.

A change of the independent variable simplifies the differential equations greatly. Starting with the state equations for the force T, we get

$$d\bar{T}/\bar{T} = \sin \pi/N \cos \phi/\cos \beta \tan(\bar{\theta} - \beta) \tag{109}$$

and using equation (105) becomes

$$d\bar{T}/\bar{T} = d\beta/\tan(\bar{\theta} - \beta) \tag{110}$$

which upon integration gives

$$\bar{T} = c/\sin(\bar{\theta} - \beta) \tag{111}$$

Boundary condition at $\phi = 0$ is

$$\bar{T} = \bar{T}_o$$

$$\theta = \theta_{min} \tag{112}$$

$$\beta = 0$$

which gives the following equation for $0 \leq \phi \leq 90^o$

$$\bar{T} = \bar{T}_o \sin \bar{\theta}_{min}/\sin (\bar{\theta}_{min} - \beta) \tag{113}$$

Recalling that the control variable switches to $\bar{\theta}_{max}$ at $\phi = 90^{o}$ gives the following boundary conditions

$$\bar{T}^{-}_{\phi=90^{o}} = T^{+}_{\phi=90^{o}} \tag{114}$$

$$\theta = \theta_{max}$$

$$\beta = \pi/N$$

and the expression for $\bar{T}$ becomes

$$\bar{T} = \bar{T}_{\phi=90^{o}} \sin(\bar{\theta}_{max} - \pi/N)/\sin(\bar{\theta}_{max} - \beta) \tag{115}$$

A solution for $\bar{R}$ is derived next

$$d\bar{R}/d\phi = \bar{T} \cos \phi \sin \bar{\theta}/(2 \bar{C}_{p} \bar{R} \sin(\bar{\theta} - \beta) \tag{116}$$

and using equations (105, 111 and 116) gives

$$\bar{R}\, d\bar{R} = c \sin \bar{\theta} \cos \beta\, d\beta/(2 \bar{C}_{p} \sin \pi/N \sin^{2}/(\bar{\theta} - \beta))$$

Again restricting to constant pressure, the integration gives

$$\bar{R}^{2} = \frac{c \sin \theta}{\sin \pi/N} (\cos \bar{\theta}/\sin(\bar{\theta} - \beta) - \sin \bar{\theta}\, \ell n \tan(\frac{\bar{\theta} - \beta}{2})) + c_{1} \tag{117}$$

where the first constant is from the T equation.

Boundary conditions at $\phi = 0$ are the same as previously defined but with the addition

$$\bar{R} = \bar{R}_o$$

The resulting equation is

$$R^2 = R_o^2 + [\bar{T}_o \sin^2 \bar{\theta}_{min}[\cos \bar{\theta}_{min}/\sin(\bar{\theta}_{min} - \beta) - \sin \bar{\theta} \ln \tan (\frac{\bar{\theta}_{min} - \beta}{2})] \sin \pi/N] - [\bar{T}_o \sin \bar{\theta}_{min}[\cos \bar{\theta}_{min} - \sin^2 \bar{\theta}_{min} \ln \tan \bar{\theta}_{min/2}]/\sin \pi/N \quad (118)$$

and at $\phi = 90^\circ$ the same expression is used with the following substitutions

$$\bar{\theta}_{min} \rightarrow \bar{\theta}_{max}$$

$$\bar{R}_{\phi=0} \rightarrow \bar{R}_{\phi=90^\circ} \quad (119)$$

$$\beta \rightarrow \pi/N$$

as was done in the T equation. Only one other variable is needed

to describe the shape, either S or Z. The latter was chosen and its differential equation is

$$d\bar{Z}/d\phi = \sin \phi \sin \bar{\theta}/(2 \bar{R} \sin^2(\bar{\theta} - \beta) \tag{120}$$

Again, writing in terms of the new independent variable β gives

$$d\bar{Z}/d\phi = \sin \beta \sin \bar{\theta} \bar{T} \cos \beta/(2 \bar{C}_p \bar{R} \sin(\bar{\theta} - \beta)) \tag{121}$$

Substituting equation (111) for T and assuming constant pressure, results in

$$d\bar{Z}/d\beta = \sin \beta \sin \bar{\theta} C_1 \cos \beta((2 \bar{R} \sin(\bar{\theta} - \beta)) \tag{122}$$

and using equation (118) for $\bar{R}$

$$d\bar{Z}/d\beta = \sin \beta \sin \bar{\theta} \cos \beta/\sin(\bar{\theta} - \beta)[\sin \bar{\theta}($$

$$\cos \bar{\theta}/\sin(\bar{\theta} - \beta) - \sin \bar{\theta} \ln \tan(\frac{\theta - \beta}{2}) + C_3]/\sin(\bar{\theta} - \beta) \tag{123}$$

The constant C_1 from the T equation and C_2 from the R equation are combined to give C_3. It is not apparent that a closed form solution is possible for this equation.

If $\bar{\theta}$ is allowed to be larger than 90°, then the solution of the problem becomes quite different. The maximum possible angle before

gores would meet is

$$\bar{\theta} = \pi/2 + \beta \tag{124}$$

Recalling the previously defined expression for the Hamiltonian, we see that for a maximum H we get

$$\bar{\theta} = \bar{\theta}_{max} \tag{125}$$

where $\bar{\theta}_{max}$ is a function of the independent variable (ref. 10). A major difference for this control law is that it does not switch at $\phi = 90^{\circ}$ in order to remain a maximum but remains constant. The resulting gore shape has a similar shape as the optimized C_D gore.

In figure 16 is shown the control variable law for maximum drag for the two control policies.

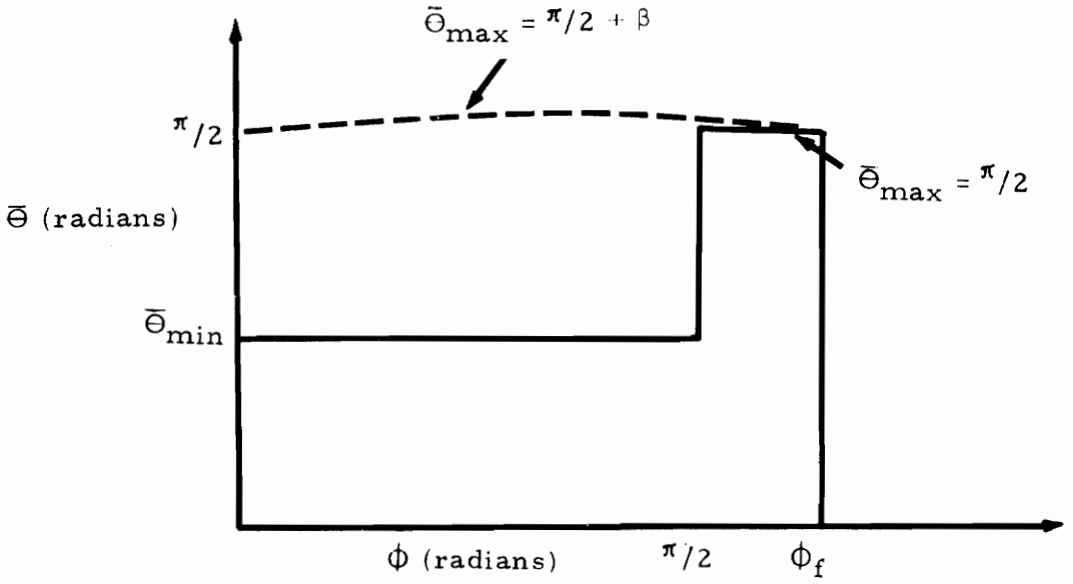

Figure 16.- Maximum drag control variable policy.

4.2 Rayleigh-Ritz Method

The basis for this method is the assumption that the minimization function can be replaced with a series approximation (ref. 8, 11). Thus, an approximate control law is known and the differential equations can be integrated, although an iterative type solution may still be required to satisfy the boundary conditions. Changes in the performance index due to small perturbations of the series coefficients are used to calculate partial derivatives of the objective function. With the gradients known, the new coefficients are determined by the method of steepest descent in the same manner as a regular max-min problem. Let the approximation of $\bar{\theta}$ be

$$\bar{\theta} = \sum_{i=0}^{3} V_i \cos \frac{i\pi}{2} \phi + \sum_{i=4}^{5} V_i \sin[(\frac{i-3}{2}) \pi\phi] \tag{126}$$

or an alternate series would be

$$\bar{\theta} = \sum_{i=0}^{5} V_i[\phi]^i \tag{127}$$

A limit is imposed by the following constraint

$$\bar{\theta}_{min} \leq \bar{\theta} \leq \bar{\theta}_{max} \tag{128}$$

and when the bounds are exceeded, the control is "trimmed" at the boundary; that is, when

$$\bar{\theta}(\phi) > \bar{\theta}_{max}$$

then $\bar{\theta}$ is set to $\bar{\theta}_{max}$. The same procedure is used for $\bar{\theta}_{min}$. Writing the performance index as

$$J = \int_{\phi_i}^{\phi_f} L(\dot{x}_i, x_i, \phi, \bar{\theta}) d\phi \tag{129}$$

along with the constraint differential equations

$$\dot{x} = f_i(x_i, \bar{\theta}, \phi) \tag{130}$$

the necessary conditions for a minimum are

$$\partial J/\partial V_i)_{i=1,5} = 0 \tag{131}$$

Unfortunately these equations cannot be solved directly; however, a numerical solution is possible.

The procedure for the solution proceeds as follows. First, the equations are integrated numerically with an assumed trial control function and the performance index recorded for use as a baseline. Next, the coefficients are changed sequentially and differential equations numerically integrated for each change. Thus, the partial derivatives of the performance index can be determined. Improvements of the control approximation are found by the steepest descent, or

$$dV_i = -K\ \partial J/\partial V_i \quad i=1,5 \tag{132}$$

and for the next iteration cycle, the coefficients are changed to

$$V_{i_{n+1}} = V_{i_n} + dV_{i_n} \quad i=1,5 \tag{133}$$

This process is repeated until the value J_{n+1} is sufficiently close to J_n in which case, for all practical purposes, the sequence has converged.

A terminal constraint may be added to the performance index. This could be written

$$J = \int L(\dot{x}_i, x_i, \phi, \bar{\theta})d\phi + K_2\psi_f^2(x_i) \tag{134}$$

However, the constant K_2 is difficult to estimate, and for the problem studied in this research, led to uncertainty in the results. As mentioned earlier, to overcome this, the iteration on the constraint was taken outside the optimization of the control variable; that is, a series of optimal problems were solved. In effect, an optimization problem within an optimization problem was obtained. For the outer loop, the method of regular steepest descent was used.

This method is rather straightforward, especially when there is no terminal constraint, and it compares very favorably with results from the method of steepest descent in functional space. A flow diagram for the main program and subroutines are shown in figures 17 and 18.

4.3 Steepest Descent Solution

The solution to an optimization problem using a direct integration approach is usually only obtainable for the simplest types of problems. Direct numerical methods have been used for a number of years in solving these types of problems, in particular, nonlinear programing. Numerous numerical schemes have been devised. One that has been used extensively is the steepest descent, or the gradient method (refs. 9, 11, 29). This technique is an iterative process that perturbates about an initial trial solution. A small change in the control variable $\bar{\theta}$ is sought that decreases the objective function. As the process is repeated, the control variable law is obtained such that the objective function ceases to change significantly for a converging system.

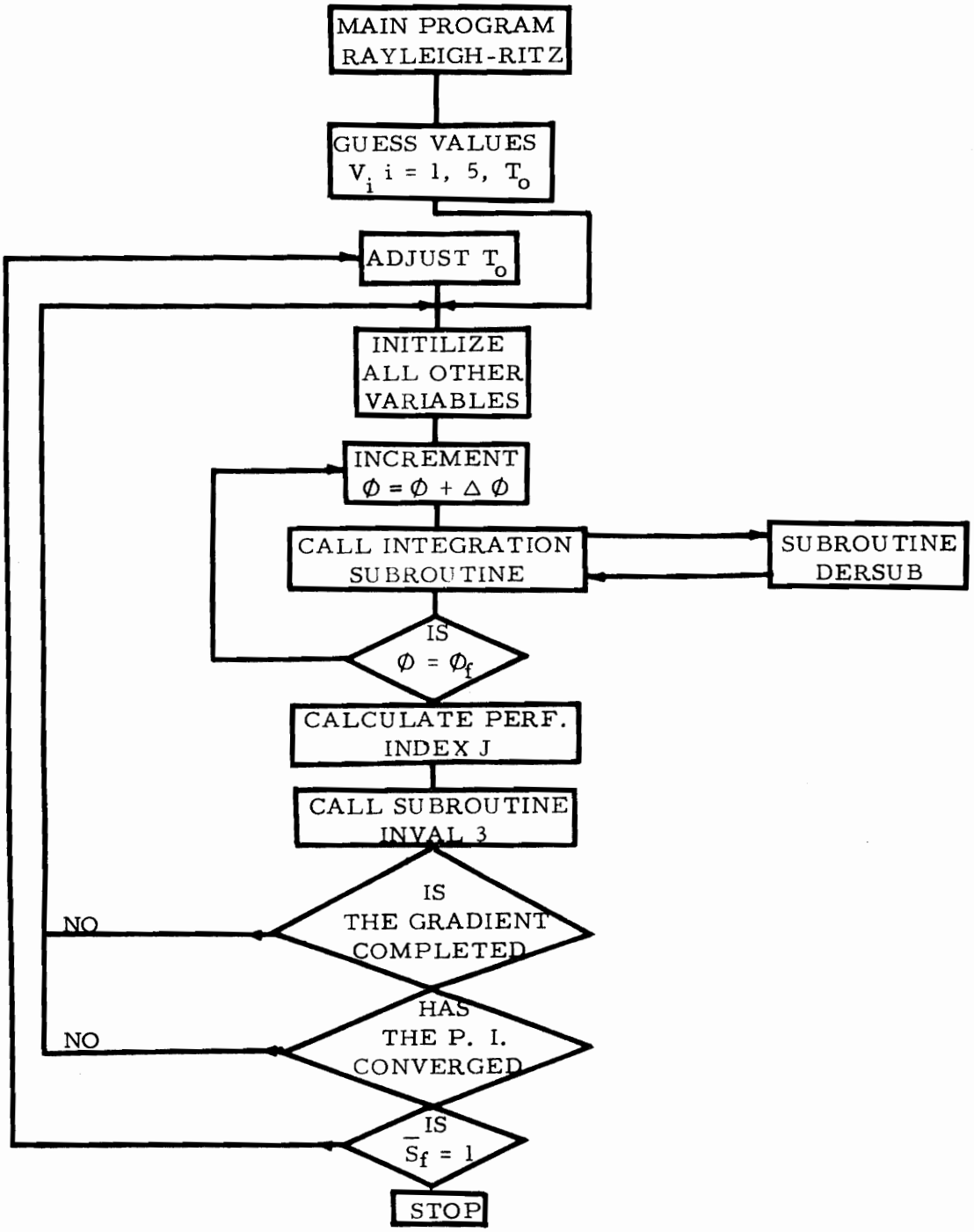

Figure 17.- Main program Rayleigh-Ritz method.

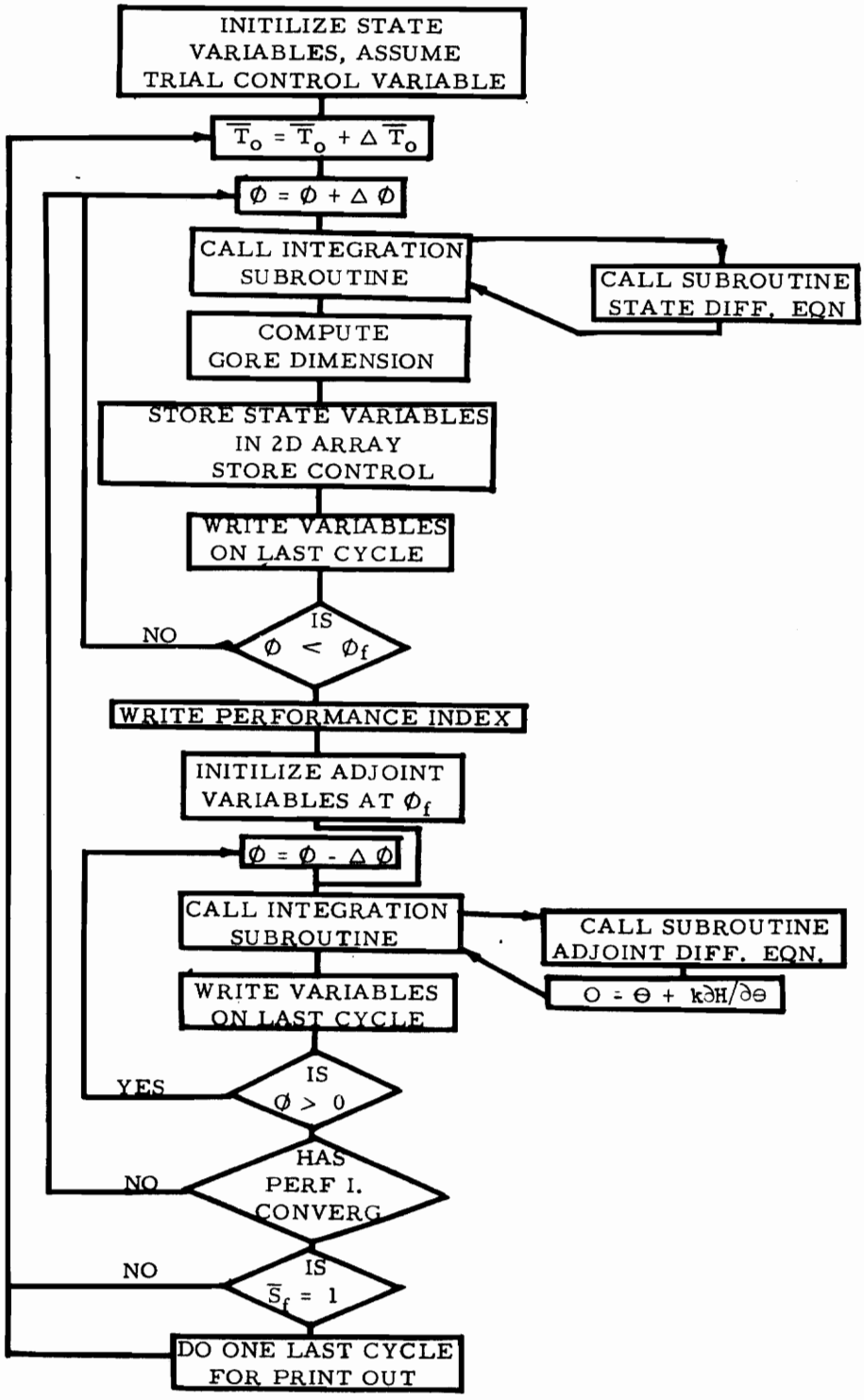

Figure 18.- Subroutines for Rayleigh-Ritz method.

A numerical solution to this problem can be outlined as follows. The performance index is selected to be the Mayer type and for the maximum drag case becomes

$$\Phi = -\bar{T}_f \sin \phi_f \tag{135}$$

and for the maximum drag coefficient

$$\Phi = -\bar{T}_f \sin \phi_f/\bar{A} \tag{136}$$

a trial control law is selected to be

$$\bar{\theta}(\phi) = \bar{\theta}_1(\phi) \tag{137}$$

For the case when there is a terminal constraint, this control satisfies the constraint. Next, the state equations are integrated forward using this control law.

A Taylor series expansion about an optimal trajectory has been derived, and using the same expansion about the trial solution gives the following

$$\delta J = -\int \frac{\partial H}{\partial \bar{\theta}})_{\text{nonoptimal}} \delta_\theta \, d\phi \tag{138}$$

$$\partial H/\partial x)_{\text{nonoptimal}} = -\dot{\lambda} \tag{139}$$

$$\partial H/\partial\bar{\theta})_{\text{nonoptimal}} \neq 0 \tag{140}$$

Thus, equation (139) is an adjoint differential equation and equation (140) provides the gradient. These equations are the same as derived in the direct solution, although it should be noted that the perturbation is about a nonoptimal trajectory. When there is a terminal constraint, the cost function is written

$$\Phi^* = \Phi + \frac{1}{2} C[\bar{R} + \bar{L}_S(1 + \bar{T}_f/\bar{E}_{SL}) \cos \phi_f]^2 \tag{141}$$

where the constraint is added as a constant times a penalty function. A variation of Φ^* gives

$$\delta\Phi^* = (\partial\Phi/\partial x)^T\delta x + C(\bar{R} + \bar{L}_S(1 + \bar{T}_f/\bar{E}_{SL})\cos \phi_f \left(\delta\bar{R} + \frac{\bar{L}_S \cos \phi_f \, \delta\bar{T}}{\bar{E}_{SL}}\right)) = 0 \tag{142}$$

which requires that the terminal conditions for the adjoint variables at $\bar{\phi}_f$ be

$$\begin{Bmatrix} \lambda_S \\ \lambda_R \\ \lambda_Z \\ \lambda_T \\ \lambda_A \end{Bmatrix} = \begin{Bmatrix} 0 \\ 0 \\ 0 \\ \sin \phi_f/\bar{A}_f \\ -\bar{T}_f \sin \phi_f/\bar{A}_f^2 \end{Bmatrix} + C \begin{Bmatrix} 0 \\ (\bar{R} + \bar{L}_S(1 + \bar{T}_f(\bar{E}_{SL})\cos \phi_f \\ 0 \\ (\bar{R} + \bar{L}_S(1 + \bar{T}_f/\bar{E}_{SL})\cos \phi_f) \dfrac{\bar{L}_S \cos \phi_f}{\bar{E}_{SL}} \\ 0 \end{Bmatrix} \tag{143}$$

for the drag coefficient objective function and a terminal constraint requiring the suspension line to intersect the axis of revolution.

Now that the terminal conditions of the adjoint variables are known, the adjoint differential equations can be integrated backward to ϕ_o.

For the next iteration cycle, the control law is

$$\theta_{n+1}(\phi) = \theta_n(\phi) + k(\phi) \frac{\partial H}{\partial \theta}(\phi) \tag{144}$$

Thus, the change in the control variable should be in the direction of the gradient for maximum change. There are various ways of selecting the function $k(\phi)$. It is necessary that $k(\phi)$ be small enough to insure that the perturbation solution remains in the linear range; however, at the control boundaries, it must be set equal to zero to prevent violating control constraints. Several methods have been suggested for selecting the function; one such method suggests that the control be written

$$\delta_\theta = \theta_{n+1} - \theta_n = k(\phi) \frac{\partial H}{\partial \theta} = \frac{a}{w(\phi)} \frac{\partial H}{\partial \theta} \tag{145}$$

where $w(\phi)$ is a weighting function. During this study the weighting function was constant and the a term was computed from

$$a^2 = k^2 / \int_{\phi_o}^{\phi_f} (\partial H/\partial \theta)^2 \, d\phi \tag{146}$$

Actually, after the first cycle, the k factor is only increased a small fraction of that indicated in equation 146 in order to remain stable. During this research it was difficult to find the correct ratio of the constants k and c and the constraint condition was eliminated by changing the independent variable to ϕ. A flow diagram of the computer program is shown in figure 19.

4.4 Results and Discussion

Several techniques are used to arrive at solutions for two different performance indexes. By taking different approaches and comparing the results with a "partial" closed form solution, confidence was gained in the accuracy. The two performance indices considered were the drag force and the drag coefficient.

The first of these is a much simpler problem and will be dealt with first. As was shown earlier, the control law equation for this case is such that closed form solution for the tape force is

$$\bar{T} = \bar{T}_o \sin \bar{\theta}_{min} / \sin(\bar{\theta}_{min} - \beta) \tag{147}$$

Since the initial force is arbitrary, it is treated as a parameter. The following values were obtained for two angles

$$\begin{aligned} \bar{T}_{90^o} &= 2.787611\ \bar{T}_o \\ \bar{T}_{100^o} &= 2.787008\ \bar{T}_o \end{aligned} \tag{148}$$

Results from the steepest descent solutions were

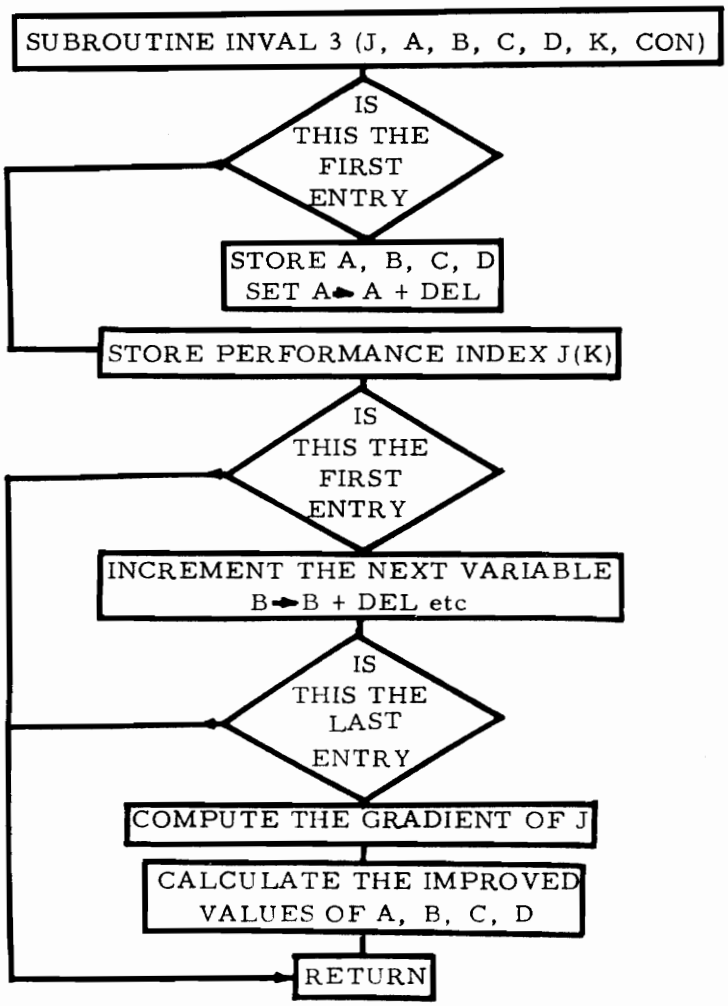

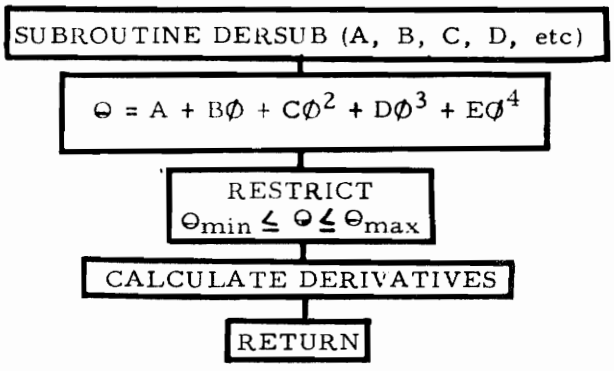

Figure 19.- Steepest descent flow diagram.

$$\bar{T}_{90^\circ} = 2.7871887\ \bar{T}_o$$

$$\bar{T}_{100^\circ} = 2.7856949\ \bar{T}_o \tag{149}$$

If it is desired to have the normalized variable $\bar{S}$ equal to unity at the terminus, then the $\bar{T}_o$ should be

$$\bar{T}_o = .119543375 \tag{150}$$

This can be derived from the normalization parameter of the force

$$\bar{T} = T/(C_{p_1}\ Q\ S_L^2\ \sin\ \pi/N) \tag{151}$$

and the variable $\bar{S}$

$$\bar{S} = S/S_L \tag{152}$$

combining these gives

$$\bar{T}_o = T_o\ \bar{S}_f^2/(C_{p_1}\ Q\ \sin\ \pi/N\ S_f^2) \tag{153}$$

Since the coefficient is an arbitrary constant, it is seen that the force varies as the square of the distance $\bar{S}_f$. For $\bar{S}_f = 1$, we can find the value of the coefficient from equation (153).

A comparison of the maximum radius can also be made since a closed form solution is available; that is,

$$\bar{R}_{max} = .5777128 \tag{154}$$

and by the method of steepest descent the results are

$$\bar{R}_{max} = .56177882 \tag{155}$$

Thus, reasonably good agreement is obtained by the method of steepest descent. It so happens that this performance index provided a control law that allows for some of the variables to be solved in closed form; however, when considering the drag force coefficient, a closed form solution does not appear likely. A further evaluation of the steepest descent method was made by comparing results with Rayleigh-Ritz method.

If $\bar{\theta}_{max}$ is allowed to be $90^{\circ} + \beta$, then the tape force is constant when β can be replaced with small angle assumptions. For constant pressure the actual change is

$$\bar{T}_f = 1.000029\ \bar{T}_o \tag{156}$$

and for variable pressure

$$\bar{T}_f = 1.005659\ \bar{T}_o \tag{157}$$

which shows that the drag performance index is not greatly dependent on the pressure distribution.

Convergence of the steepest descent method is quite reliable, and from figure 20 can be seen the rate of convergence. The control angle was input at a constant value of 50°, and after 49 iterations, the change in the performance index was less than 6×10^{-8}. Also included in the iteration cycle was the terminal boundary condition

$$\bar{S}_f = 1 \tag{158}$$

which had converged to ≈ 1.

The Rayleigh-Ritz method approximates the control variable with a series approximation. Both polynomial and trigonometric series were used, and the results indicate that the trigonometric series gives a slightly higher performance.

The results using this method compare favorably with the steepest descent technique. In the table below can be found the gore dimensions determined by the two methods. Two series approximations were used. For a trigonometric series, the expression was determined to be

$$\theta = .41305715 + .16020063 \cos \frac{\pi\phi}{2} - .40930817 \cos \pi\phi + .03999156 \sin \frac{\pi\phi}{2} - .1112364 \sin \pi\phi \tag{159}$$

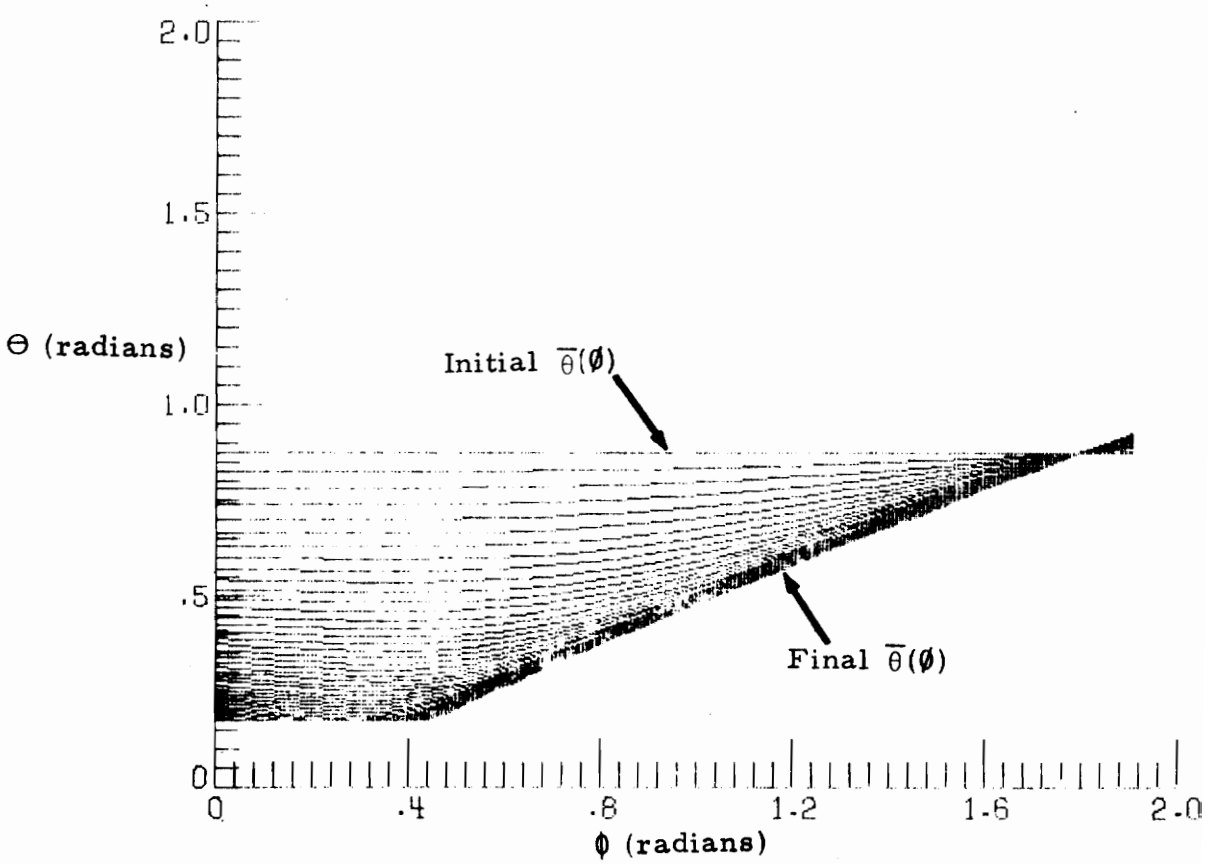

Figure 20.- Convergence of steepest descent.

and for the polynomial expression

$$\theta = -.03064917 + .73902907\ \phi + .50361075\ \phi^2 + .014047536\ \phi^3 - .33029901\ \phi^4 \qquad (160)$$

TABLE 2

Comparison of Steepest Descent with Rayleigh-Ritz

Independent Variable	Steepest Descent D/2	Rayleigh-Ritz D/2	Gore Center Line Distance
0	.012508	.012508	.099365
.0976	.02252	.022448	.19843
.1951	.030491	.030382	.2693
.2927	.037364	.037223	.33172
.3902	.043708	.043539	.39107
.4878	.049774	.049574	.44961
.5854	.055300	.055099	.50425
.6829	.060171	.059996	.55462
.7805	.064496	.0643518	.60147
.8780	.068337	.068229	.64534
.9756	.071736	.071674	.68664
1.0732	.074722	.074723	.72571
1.1707	.077327	.077400	.76280
1.2683	.079556	.079718	.798134
1.3658	.081443	.0816818	.831895
1.4634	.083002	.083287	.86424
1.5610	.084249	.084522	.895316
1.6585	.085202	.085367	.92524
1.7561	.085876	.085796	.954108
1.8536	.086287	.085783	.98203
1.9024	.086397	.085608	.99566

5.0 COMPARISON OF OPTIMIZED WITH EXISTING PARACHUTES

A basic reference has been established by analyzing existing parachutes from which the performance of the optimized parachute can be evaluated. We see that the optimized gore shape is somewhere between the flat circular and extended skirt. It more closely follows the 1/4 sphere than any of the other parachutes. The performance index increases slightly over the other designs.

A comparison of the drag coefficient of several existing parachutes was shown in table 3. The optimized parachute is now compared with the other parachutes, also the recommended C_D taken from reference 3 is included.

TABLE 3

Drag Coefficient of the Optimized Parachute Compared With Existing Designs

Type parachute	Calculated C_D	Reference 3 preliminary design values
Optimized	.695	-
1/4 sphere	.675	.65 - .85
Extended skirt	.645	.65 - .85
Conical	.681	.62 - .95
Flat circular	.640	.65 - .95

From this comparison, it is obvious that there is much uncertainty in the measured drag coefficients. Such things as oscillatory forces, gliding, cloth porosity, skin friction, suspension line length, and magnitude of the terminal velocity all add to the variations. The analytical results show the differences due to pressure forces only. Of significance is the relative magnitudes, and not absolute values since it is desired to improve existing designs.

5.1 Comparison of Shapes

A plot of the gore shapes is shown in figure 22 where the subtle differences between the optimized and current designs can be evaluated. In the region near the vent there is very little difference, whereas, near the skirt the optimized design follows the 1/4 sphere closely. Also, in this region, the extended skirt tends to decrease the lobing just as the optimized parachute. In general, the results show that improvement in drag coefficients of existing parachutes could be improved by decreasing lobing in the outer region.

For the maximum drag design, two solutions were obtained. When $\bar{\theta}$ is limited to 90°, the control law switches to a minimum at the maximum radius. However, if the maximum θ is allowed to be $90^{\circ} + \beta$, then the control law states that $\bar{\theta}$ remains constant at its maximum limit.

The first control law mentioned above was arrived at by three methods, that is, the maximum principle, steepest descent, and the Rayleigh-Ritz method. When comparing the resulting drag force with other parachutes, it was obvious that this was not an optimum design.

By allowing the control variable to increase by the additional angle β, the maximum drag design was found. The resulting gore shape is similar to the 1/4 sphere but has more fullness.

As noted in reference 3, the maximum drag coefficient is obtained when the ratio of the deployed diameter to the constructed diameter is a maximum. This can be determined when comparing the deployed shapes of figure 21 with the maximum gore dimensions shown in figure 22.

Also included in this figure is the profile of the maximum drag parachute. This parachute has the greatest inflated diameter, thus, having more surface area with an attendant reduction in C_D, even though it has a high drag force.

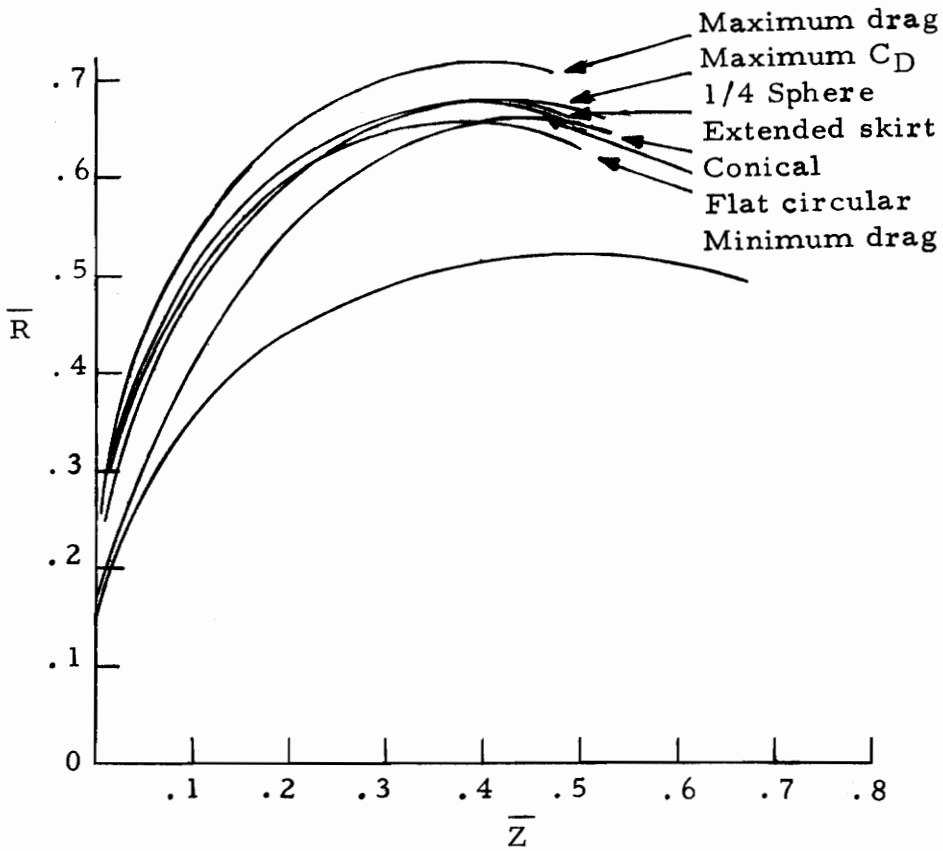

Figure 21.- Deployed shapes.

A comparison of gore shapes can be seen in figure 21 where 1/2 the gore width versus the meridional distance is shown. The optimum parachute is similar to the 1/4 sphere with the major difference being a reduction in fullness in the region of the skirt. By comparing the extended skirt design with the other parachutes, we see that a correction is made to reduce the excess material. The conical parachute is an obvious compromise and has a good drag coefficient, although relatively high stresses would occur in the mid-region.

5.2 Major Influencing Parameters

In this section the primary factors influencing the optimized design are investigated. The following parameters were studied: pressure variations, suspension line length, skirt angle ϕ, structural flexibility, and strain in the radial tapes.

Pressure distribution assumptions have a significant influence on the optimized design. In figures 23, 24, and 25 can be seen the effect of constant and variable pressure distributions on the resulting shape. There is a need to design more fullness in the outer regions for variable pressure. Drag coefficients for the two designs are: $C_D = .659$ constant pressure, and .695 for variable pressure. In both cases, the structural flexibility was selected to be infinite in order to compare pressure influences only.

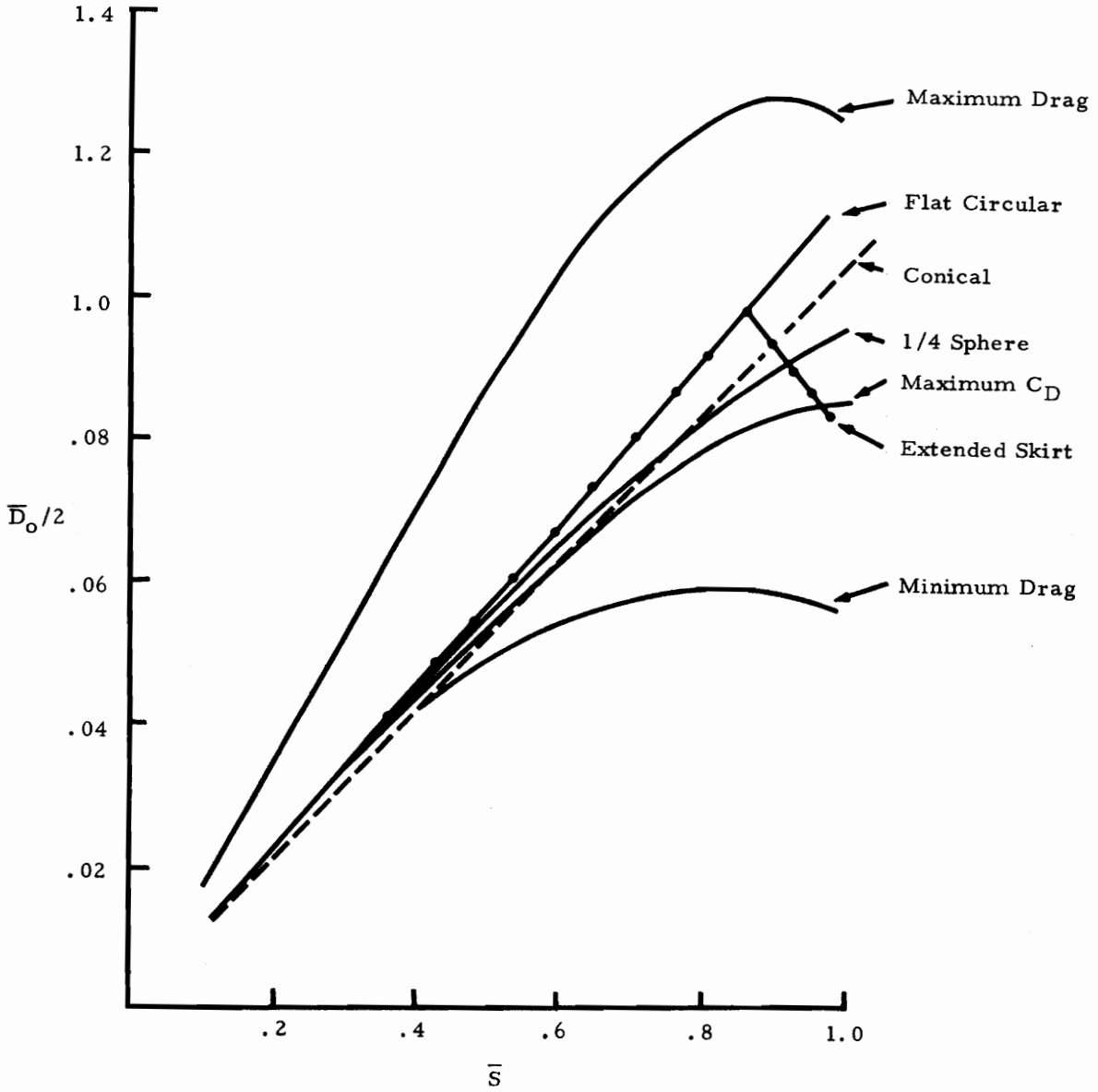

Figure 22.- Comparison of gore shapes.

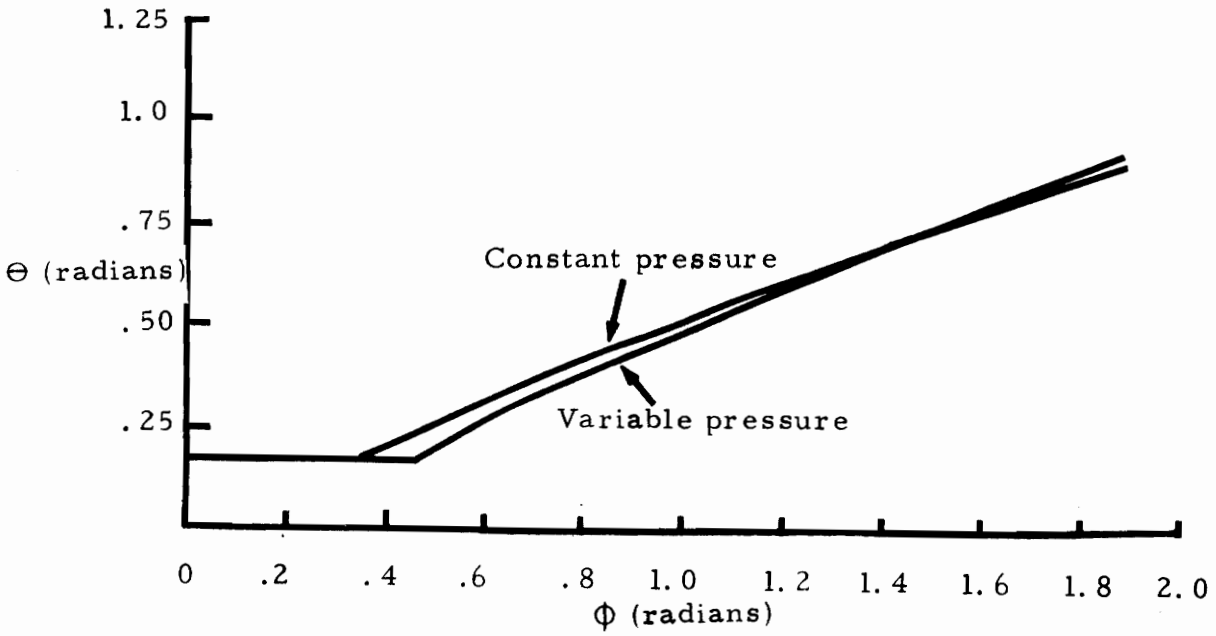

Figure 23.- Effect of pressure distribution on control variable.

Structural flexibility influences the optimum design in two areas; that is, both the meridional member and secondary membrane stretching structure needs to be considered. The meridional members are fabricated to preclude any significant canopy stress, and is accomplished by either preloading the tapes when making measurements for construction or by designing the tapes shorter than the meridional length of the secondary structure. In either case, the meridional stress in the membrane is essentially zero and is assumed to be negligible. The stretching in the hoop direction has the effect of

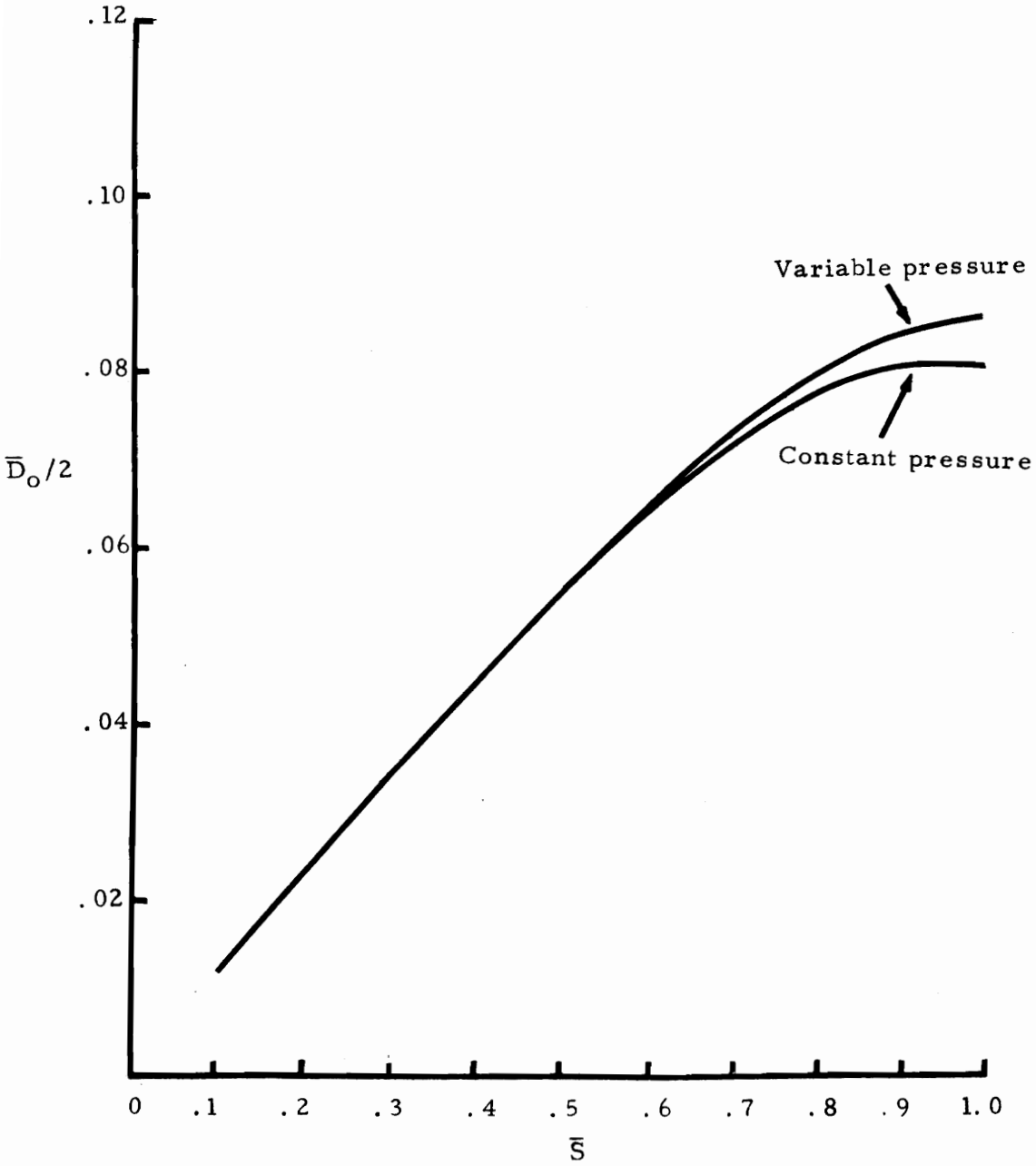

Figure 24.- Effect of pressure distribution on gore shape.

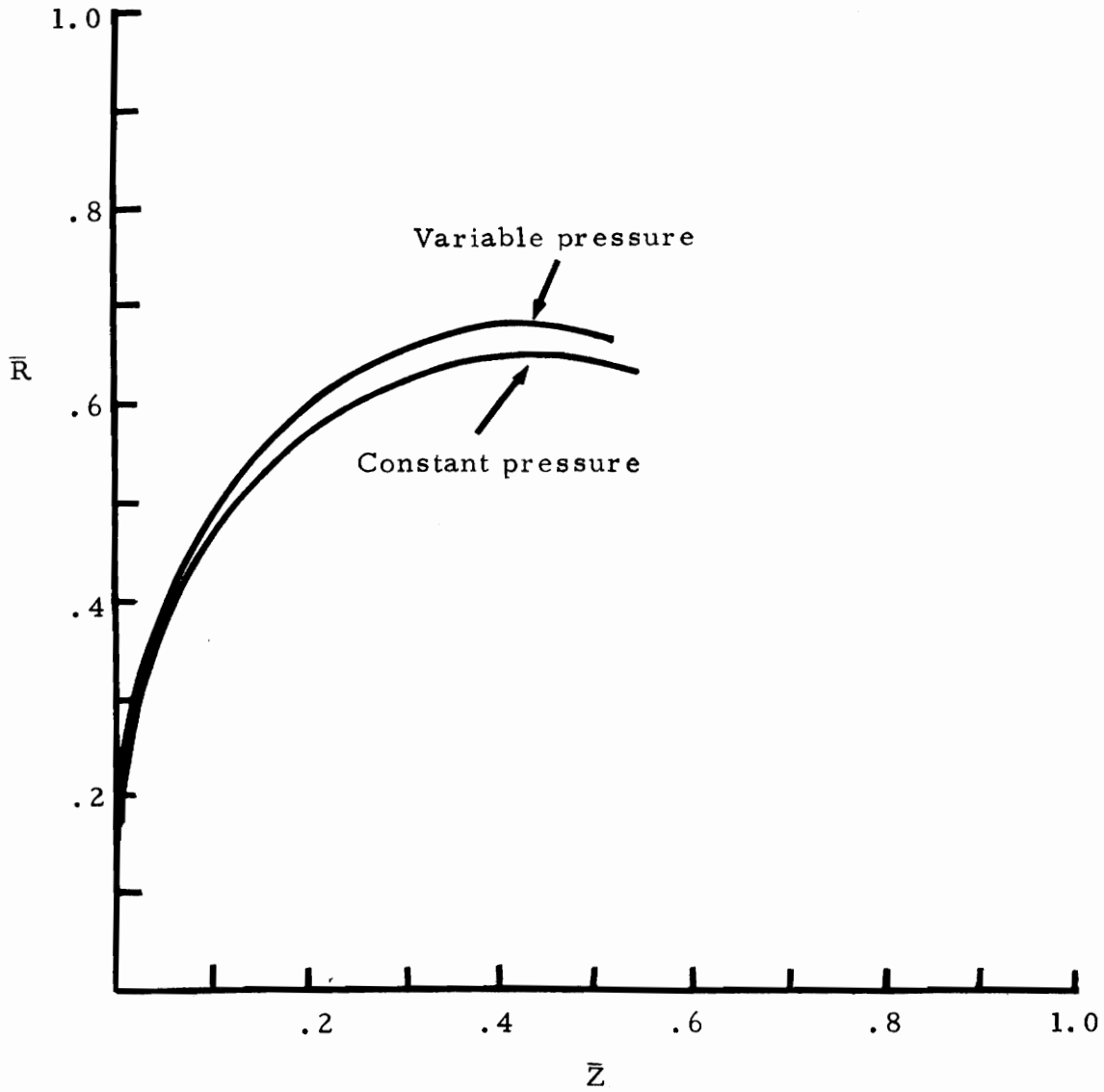

Figure 25.- Effect of pressure distribution on deployed shape.

increasing the canopy area, and therefore, the drag coefficient. A parameter study showing this influence is shown in figure 26. It can be seen from this figure that there is a slight increase due to flexibility, but to become of major importance, has to be much more flexible than current parachute design materials. This factor is governed primarily by required strength capability at this time.

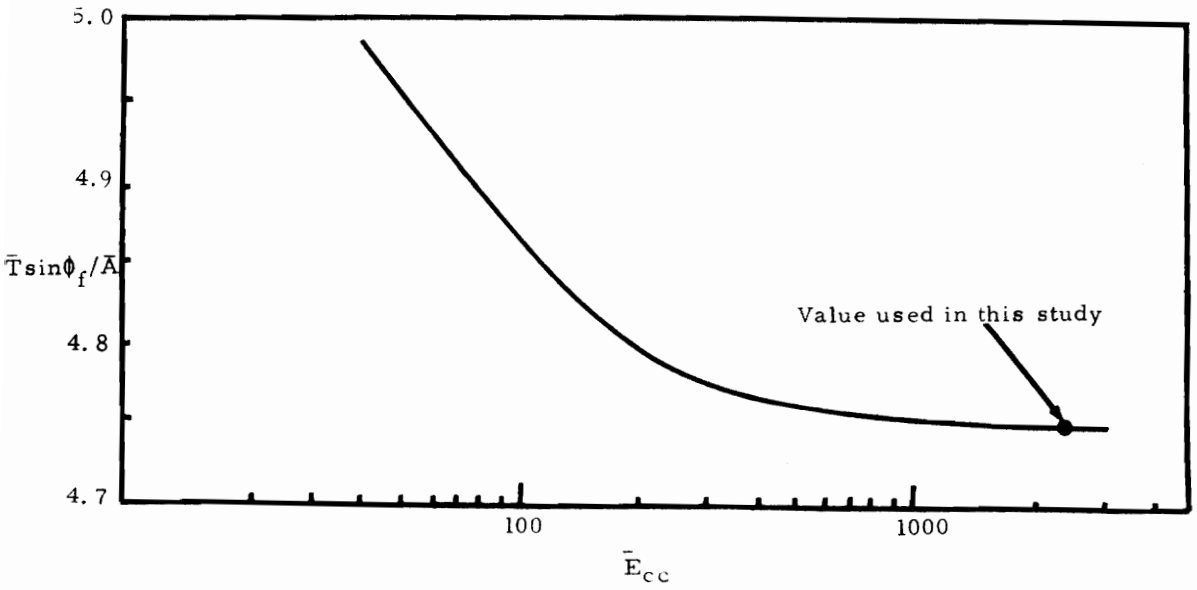

Figure 26.- Effect of membrane stiffness on drag.

A significant parameter in the optimized design is the length of the suspension lines. This length is determined by the radius and the angle of the independent variable ϕ_f at the skirt. Using equation (43) and solving for $\bar{L}_s$ gives

$$\bar{L}_s = \bar{R}_f/(1 + \bar{T}_f/E_s)\cos \phi_f \qquad (161)$$

A plot of this curve is shown below

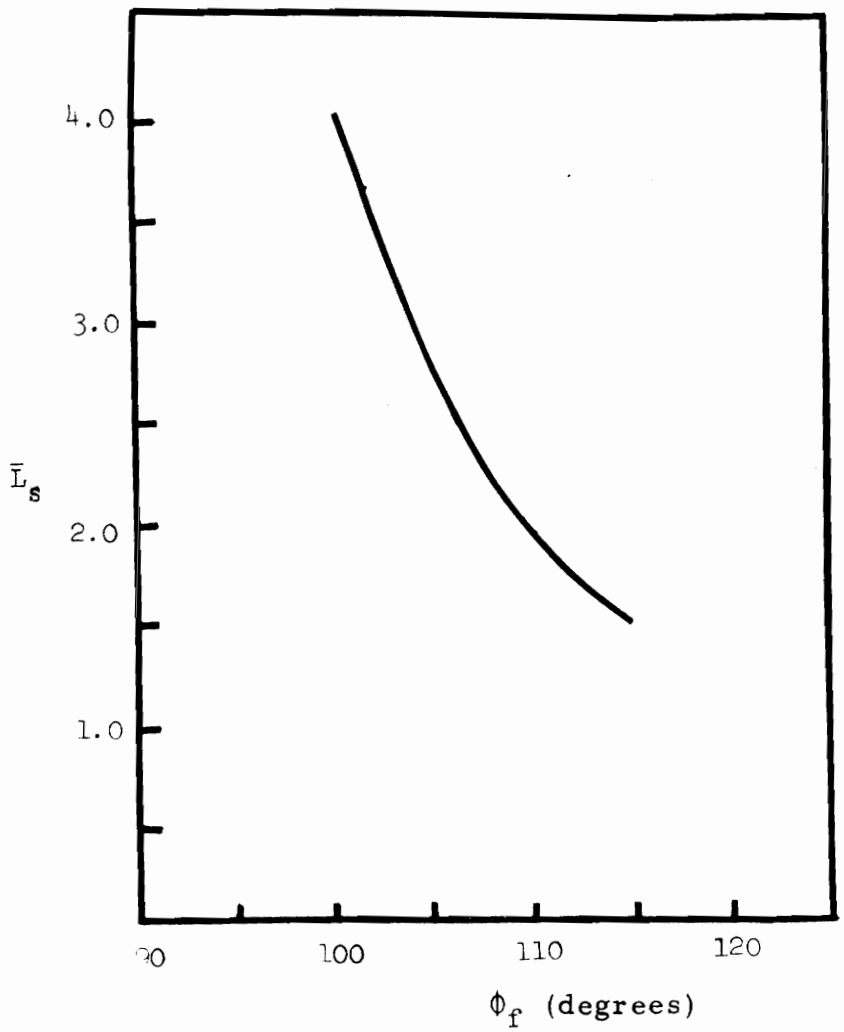

Figure 27.- Effect of skirt angle on suspension line length.

A frequent design condition of parachutes is

$$\bar{L}_s = 2\bar{S}_f \tag{162}$$

which gives an angle of

$$\phi_f = 109.371 \tag{163}$$

for the optimized design. Photographs of parachutes during flight indicates that this angle is 109° for a flat circular parachute (ref. 31).

The drag coefficient is also a function of the skirt angle ϕ_f. It is assumed in all of these parameter studies that the pressure distribution is not changed when ϕ_f varies. The influence of this assumption on the performance index is unknown since no data are available for evaluation. In figure 28 is shown the functional relationship between the drag coefficient and ϕ_f.

The optimum shaped gore is based on the premise that the canopy meridional stress is negligible and is accomplished by shortening the primary meridional members. Calculated stretch required for this condition is found from equation (15).

$$r_\phi \, d\phi = (1 + \varepsilon_\phi) dS \tag{164}$$

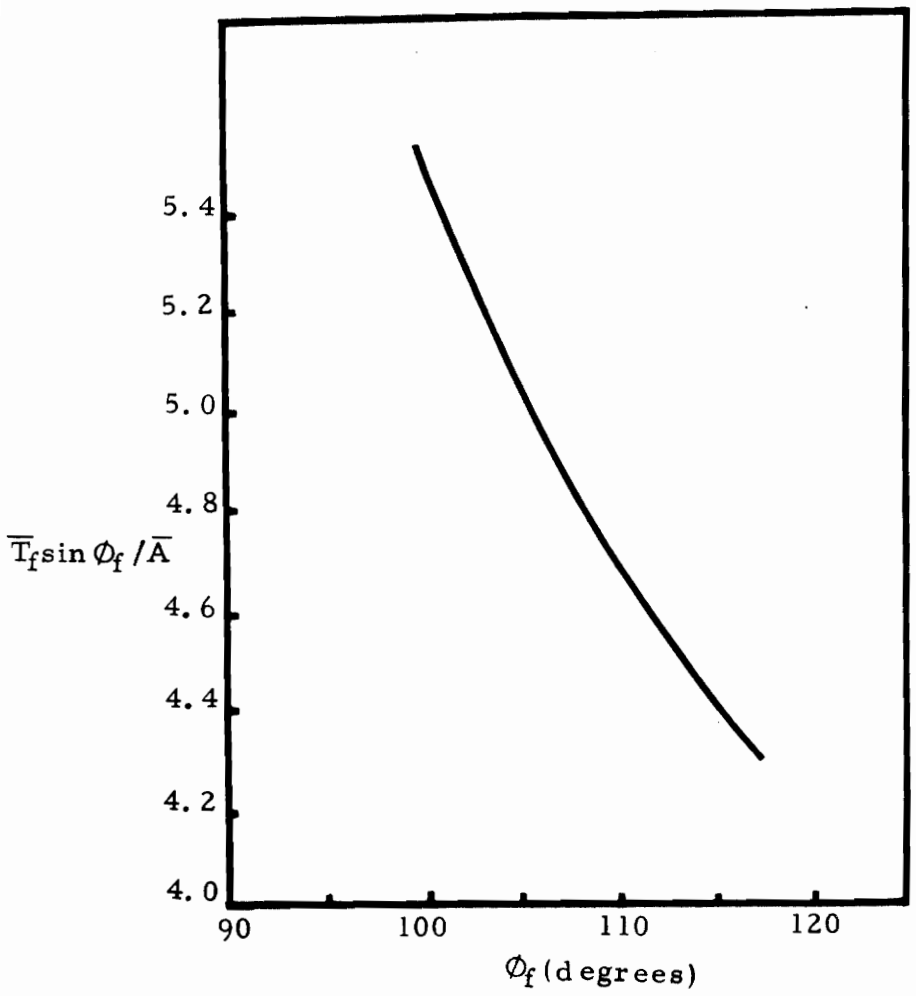

Figure 28.- Effect skirt angle on drag coefficient.

A plot of the tape strain distribution is shown below.

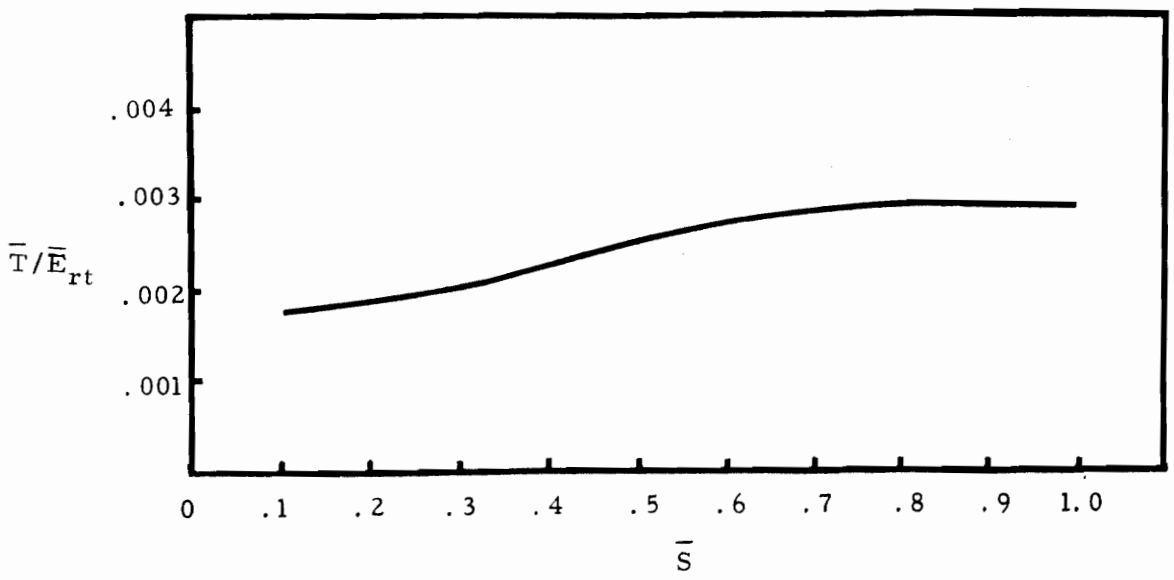

Figure 29.- Radial tape strain.

The integration shows the total stretch to be 1/4%. It should be mentioned that this is the minimum required prestretching, while other conditions such as opening shock loads could increase these values.

5.3 Results and Discussion

When the drag coefficient is optimized, the resulting parachute closely resembles current designs except near the skirt. In this region it is beneficial to reduce the canopy fullness. The optimized parachute closely follows the 1/4 spherical design that is known to have a relatively high drag coefficient.

For maximum drag the design is quite different; in that, the gore fullness is a maximum in the region near the skirt. This type of design is difficult to achieve since in-folding, or collapse, would

undoubtably occur. Past experience has shown that this problem can be dealt with by special designs near the skirt.

The maximum deployed radius is achieved by the optimum design - a well-known design objective.

Variation of the suspension line length is shown to be an important influence. Assuming that the pressure distribution is relatively insensitive to changes in the aft closure angle, it was found that increasing the suspension line length increases the drag coefficient; however, there would be a large increase in the total weight or bulk of the parachute.

Structural flexibility is a secondary effect for the canopy when considering current design loads; nevertheless, increasing flexibility increases the drag coefficient. The required radial tape stretching necessary to prevent meridional loads in the canopy is shown.

The influence of pressure distribution on the optimum design is difficult to assess. It was found during the study of existing parachutes that the distribution was similar for large variations in geometry, and would lead one to believe that the variation in pressure was relatively insensitive to the parachute shape. However, the optimized C_D parachute was shown to be dependent on the assumed pressure. This relationship is unknown, and should it become important, an iterative type solution would be required.

For the maximum drag performance index, pressure distribution was insignificant since the control variable is always on the boundary.

6.0 CONCLUSIONS

Equations are derived for calculating loads in a polygonal body of revolution where the meridional stress in the secondary member is considered negligible. The primary members, or chords, transfer all of the meridional loads in the radial direction due to its length being shorter. Experimental pressure distributions are represented by a polynomial equation, that in general, fits data for several different types of parachutes. Analysis of these designs results in a two point boundary type problem.

Findings indicate a significant difference in the calculated drag coefficients for the four parachutes studied, and when comparing with recommended design values in the parachute handbook, the analysis consistently predicts low values. The difference is thought to be the result of neglecting such factors as oscillations, gliding, cloth porosity, and drag from the suspension lines. Computed inflated shapes compare very well with measured flight shapes.

The fundamental equations reduce to the Taylor curve when the number of gores increase to an infinite number and the pressure is assumed to be constant. Another interesting result is obtained when the lobing between primary members is restricted to the condition that $\theta = \beta$, the equations reduce to the membrane expression for a cone. The nondimensionalized variables indicate that structural stiffness of parachutes vary inversely with size. With the fundamental expressions for describing the loads and shapes of parachutes

established, an assessment of the validity of the optimized design can be made. It should be remembered that the merits of the optimum design are relative and should show valid trends even though the analysis is only approximate.

It is desired in this thesis to determine the effect of varying the gore geometry on the drag characteristics. The question is, given a required parachute diameter, what can be done to the gore shape to get the maximum drag and the maximum drag coefficient.

For maximum drag, two solutions were found; one law required the membrane lobing to be a minimum in the region from the vent to the maximum radius, and then switch to maximum fullness and remain constant to the skirt. This solution was determined by utilizing the Pontryagin's Maximum Principle, and a closed form solution was found for several of the differential equations. These solutions were compared with the results using numerical techniques and the agreement is considered good. The drag load arrived at using this control policy did not produce maximum drag. By changing the upper boundary on the control variable from 90° to $(90^{\circ} + \beta)$, a new control law was found that requires $\bar{\theta}$ to remain constant at $\bar{\theta}_{max}$. This did indeed produce the maximum drag load, and was corroborated using the Rayleigh-Ritz method.

When optimizing for maximum drag coefficient, the control law is a minimum in the inner region near the vent, but as the skirt is approached, the lobing increases; however, maximum fullness is not reached for this case.

It was found that pressure distribution has a significant effect on the gore shape. As the meridional distance increases, test data indicates that the pressure increases and the optimization law predicts that the fullness should also increase.

Structural flexibility of the secondary structure was found to have a minor effect for the loads encountered during the final steady-state phase. The stiffness is usually dictated by strength requirements; however, for a very flexible membrane, the increase in C_D would be significant. It was also found that the drag coefficient increases as the number of gores increase.

Comparing the optimized parachute with several current designs indicates that, in general, the optimum design has been covered. However, there is a slight increase in performance to be gained by decreasing the fullness in the skirt region of the 1/4 sphere parachute. This could be accomplished by incorporating features similar to the extended skirt design with the 1/4 sphere. That is, in the skirt region the fullness could be reduced in the same manner as the extended skirt.

For the pseudo optimum drag design, the guide surface parachute probably bears the closest resemblance. A description of this design is given in the "Parachute Handbook" where its virtues are given as: excellent stability and good opening characteristics. The true optimum drag parachute is very similar to 1/4 sphere - the difference being that the fullness is greatly increased. The theoretical deployed shape of this parachute is the Taylor curve. A 6-foot model

of this design was fabricated and tested in the Langley Research Center spin tunnel. Because of excessive fullness, full inflation could not be obtained, or there was "infolding" of five gores. Further development would be necessary to overcome this problem. The addition of a device such as an extended panel could be tried.

Several methods were used in determining the optimization laws. The fastest and most straightforward technique was the steepest descent method. Convergence for the problem studied, after replacing a terminal constraint with a parameter study, was very fast.

Another method was used to gain confidence in the results from the steepest descent. This technique is the familiar Rayleigh-Ritz type solution applied to an optimization problem. Convergence is much slower for this method, although the resulting control law is very close to the one produced by the steepest descent.

The numerical techniques were not reliable for predicting the maximum drag performance law. By changing the sign on the performance index, the Rayleigh-Ritz method converged to the true maximum; however, the steepest descent failed.

7.0 REFERENCES

1. Alley, Vernon L., Jr.: A Stress Analysis of the Viking BLDT-1 Parachute Canopy With Emphasis on the Effects of Asymmetries. Langley Working Paper No. 1067, July 1972.

2. Alley, V. L., Jr.; and Faison, R. W.: Experimental Investigation of Strains in Fabric Under Biaxial and Shear Stresses. Journal of Aircraft, Vol. 9, No. 1, January 1972.

3. Anon.: Performance of and Design Criteria for Deployable Aerodynamic Decelerators. American Power Jet Company, AFFDL Technical Report No. ASD-TR-61-579, December 1963.

4. Anon.: Final Technical Report 40 Foot Diameter Ringsail Parachute; Planetary Entry Parachute Program; NASA CR-66586; Pioneer Parachute Company.

5. Anon.: Analysis of Apollo Spacecraft Parachutes. Quarterly Progress Report No. 2: NVR-6389, January 1969.

6. Asfour, K. J.: Analysis of Dynamic Stress in an Inflating Parachute. Journal of Aircraft, Vol. 4, No. 5, September 1967.

7. Ashton, J. E.: Primer on Composite Materials Analysis. Academic Press, 1964.

8. Beveridge, Gordon S. G.; and Schechteo, Robert S.: Optimization: Theory and Practice. McGraw-Hill.

9. Bryson, A. E., Jr.; and Ho, Y. C.: Applied Optimal Control. Ginn and Company, 1969.

10. Bryson, A. E., Jr.: Denham, W. F.; Dreyfus, S. E.: Optimal Programming Problems With Inequality Constraints I: Necessary Conditions for Extremal Solutions. AIAA Journal, November 1963.

11. Denn, Morton M.: Optimization by Variational Methods. McGraw-Hill, 1969.

12. DeSantis, Gregory C.: An Analysis of Parachute System Parameters. 4th AIAA Aerodynamic Decelerator Systems Conference, May 1973.

13. Eldred, C. H.; and Mikulus, Martin, Jr.: Transient Aerodynamic Pressures During Unsteady Parachute Processes. AIAA Third Aerodynamic Deceleration Systems Conference, Wright-Patterson Air Force Base, Ohio, Sept. 1970.

14. Flugge, W.; and Chou, S. C.: Large-Deformation Theory of Shells of Revolution. ASME Applied Mechanics Division, March 1967.

15. Fralich, R. W.: Stress and Shape Analysis of a Paraglider Wing. Ph. D. Dissertation, Virginia Polytechnic Institute, June 1963.

16. Gilbert, J. L.; and Bobbitt, P. J.: Comparison of Measured and Calculated Loads of a 5.5 Foot Disk-Gap-Band Parachute at Low Velocities. Proposed NASA Technical Memorandum.

17. Heinrich, H. G.; and Haak, E. L.: Stability and Drag of Parachutes With Varying Effective Porosity. ASD-TDR-62-100, 1962.

18. Heinrich, H. G.; and Jamison, L. R.: Parachute Stress Analysis During Inflation and at Steady State. AIAA Entry Technology Conference, Williamsburg, Va., October 1964.

19. Heinrich, H. G.; and Jamison, L. R., Jr.: Stress Analysis of a Parachute During Inflation and at Steady State. FDL-TDR-64-125, February 1965 (AD 461-387).

20. Heinrich, H. G.; and Noreen, R. A.: Experimental Stress Analysis on Inflated Model Parachutes. 4th AIAA Aerodynamic Decelerator Systems Conference, May 1973.

21. Houmard, J.: Stress Analysis of Viking Parachute. AIAA 4th Aerodynamic Decelerator Systems Conference, No. 73-444, May 1973.

22. Houtz, N. E.: Optimization of Inflatable Drag Devices by Isotensoid Design. AIAA Paper No. 64-437, July 1964.

23. Krause, H.: Thin Elastic Shells. Wiley, 1968.

24. Lambiotte, J. J.; and Smith, K. A.: A Series of Common Usage Computer Subroutines to Solve Simultaneous Ordinary Differential Equations. Langley Working Paper 389, April 1967.

25. Leitmann, G.: An Introduction to Optimal Control. McGraw-Hill, 1966.

26. Lester, W. G. S.: A Note on the Generalization of Elastic Curves Representing Parachute Shapes. Ministry of Aviation, Aeronautical Research Council C.P. No. 665, 1963.

27. Melzig, H. D.; and Schmidt, P. K.: Pressure Distribution During Parachute Opening. AFFDL-TR-66-10, March 1966.

28. Milulas, Martin M., Jr.: Behavior of Doubly Curved Partly Wrinkled Membrane Structures Formed From an Initially Flat Membrane. Ph. D. Dissertation, VPI and State University, June 1970.

29. Mikami, K.; Battle, T.; Goodell, R.; and Bryson, A.: Three-Dimensional Trajectory Optimization Study. ASD-TDR-62-295, Air Force Systems Command, Oct. 1962.

30. Mullins, W. M.: Stress Analysis of Spacecraft Parachutes Using Finite Elements and Large Deformation Theory. 3rd AIAA Aerodynamic Decelerator Systems Conference, Wright-Patterson Air Force Base, Ohio, Sept. 1970.

31. Ross, E. W.: Approximate Analysis of a Flat, Circular Parachute in Steady Descent. U. S. Army Tech. Report 69-51-OSD.

32. Stevens, G. W. H.; and Johns, T. F.: The Theory of Parachutes with Chords Over the Canopy. Ministry of Supply, Aeronautical Research Council Reports and Memoranda No. 2320, 1942.

33. Taylor, Sir Geoffrey Ingram: On the Shapes of Parachutes. The Scientific Papers of Sir Geoffrey Ingram Taylor, Vol. III, 1963.

34. Topping, A. D.; Marketas, J. D.; and Costakos, N. C.: A Study of Canopy Shapes and Stresses for Parachutes in Steady Descent. WADC Tech. Report 55-294.

APPENDIX A

SOLUTION OF THE THETA TRANSCENDENTAL EQUATION

During each integration step, it is necessary to solve for the angle θ. Since this iteration is inside the boundary condition iteration loop, θ must be found accurately. Several methods have been used for solving this equation, (ref. 18, 30, 31) and all have some limitations. In reference 2, the trigonometric function is expanded in a series and was used for angles up to 90^{o}, whereas, in reference 1 a Newton-Raphson method is used for large angles and a series expansion for small angles. A third method is presented in reference 30 in which a direct substitution was used. The following method has been successfully used in this research. First an approximation of theta is obtained by neglecting membrane flexibility and expanding theta in a series, or

$$\bar{\theta} = [6(1 - \ell/D_o)]^{1/2} \tag{A-1}$$

Writing the transcendental expression as

$$F = \bar{\theta} - (\sin \bar{\theta} + \bar{C}_p \bar{R}/\bar{E}_{cc})D_o/\ell = 0 \tag{A-2}$$

an expression for a solution of $\bar{\theta}$ is

$$\bar{\theta}_{n+1} = \bar{\theta}_n - \left(\frac{dF/d\bar{\theta}}{d^2F/d^2\bar{\theta}}\right)_n^2 + \left(\left(\frac{dF/d\bar{\theta}}{d^2F/d\bar{\theta}^2}\right)^2 - \frac{2F}{d^2F/d^2\bar{\theta}}\right)_n^{1/2} \quad \text{(A-3)}$$

Convergence of this equation is very fast and reliable, whereas, other methods mentioned previously have some liabilities. However, it has a limitation in that D_o has to be equal to or greater than ℓ. This is usually the case in parachute design.

Equation (4-3) is derived from the following geometric relationships, see figure 30. The width of the gore is a known function, that is

$$D_o = f_1(S) \quad \text{(A-4)}$$

Also, the span that this width must cover is given by

$$\ell = 2\pi R \sin \pi/N \quad \text{(A-5)}$$

There is also a geometric condition relating the curvature of the membrane to its stretch length.

$$\bar{\theta} = D/\ell \sin \bar{\theta} \quad \text{(A-6)}$$

where D is the stretched membrane

$$D = 2(r + w)\bar{\theta} \quad \text{(A-7)}$$

and writing in terms of the stress resultant

$$D = D_o \left(1 + N_\theta / E_{cc}\right) \tag{A-8}$$

Substituting in equation (B-2) and simplifying gives

$$\bar{\theta} = D_o / \ell \left(\sin \bar{\theta} + C_p \; Q \; R \sin \pi / N / E_{cc}\right) \tag{A-9}$$

and writing in nondimensional form

$$\bar{\theta} = \bar{D}_o / \bar{\ell} \left(\sin \bar{\theta} + \bar{C}_p \; \bar{R} / \bar{E}_{cc}\right) \tag{A-10}$$

where variables not previously defined are

$$\bar{D}_o = D_o / S_L \tag{A-11}$$

and

$$\bar{E}_{cc} = E_{cc} / C_{p_1} \; Q \sin \pi / N \; S_L \tag{A-12}$$

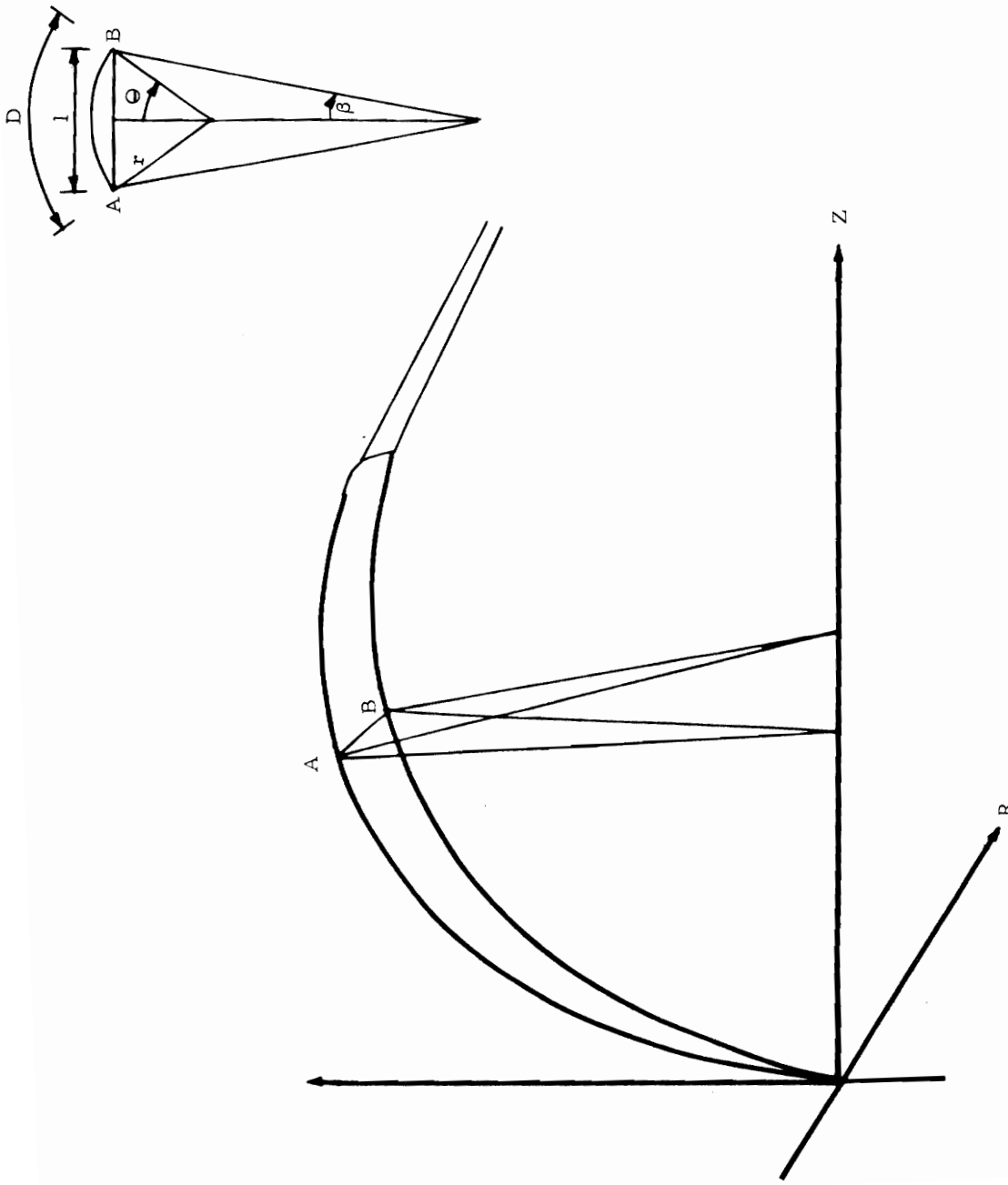

Figure 30.- Gore geometric relations.

VITA

Mr. Gilbert was born in Richmond, Virginia, on January 23, 1931. He attended Glen Allen High School in Henrico County from 1944 to 1949, and Virginia Military Institute from 1949 to 1953 where he received a Bachelor of Science Degree in Civil Engineering. Upon graduation, he entered the Air Force and served as a pilot until 1956, and after discharge returned to Virginia Military Institute as an Instructor in the Mechanical Engineering Department until 1958. He attended the University of Virginia as a Graduate Assistant before joining the National Aeronautics and Space Administration in 1959. The author received his Master of Mechanical Engineering degree in 1965 from the University of Virginia. He is a registered Professional Engineer in the state of Virginia, is married and has two children.

John L. Gilbert

OPTIMIZATION PARAMETERS FOR A MEMBRANE POLYGONAL BODY OF REVOLUTION WITH ZERO MERIDIONAL STRESS AND ITS APPLICATION TO PARACHUTES

By John L. Gilbert

ABSTRACT

A polygonal body of revolution consisting of discrete meridional members joined by regular polygons is optimized for maximum drag and drag coefficient. The meridional, or primary members, carry all of the radial loads and the membrane structure transfers applied pressure loads to the primary members. The shape of the secondary membrane is found such that the performance index is optimized.

Several methods are utilized to solve for the optimum conditions, and an application of these solutions to a parachute design is shown. The results are presented in parametric form with pressure distributions, structural flexibility, and skirt closure angle being the parameters investigated.

In general, the results verified experimental data in several areas and that the current shapes used in design cover the optimum region, although refinements could be made in some areas. Of particular significance is the difference in shape for optimum drag and drag coefficient. For maximum drag force, the fullness or the lobing between meridional members should be a maximum throughout the span of the gore, whereas, for the maximum drag coefficient design, the lobing is a minimum in the region near the vent and gradually increases as the

meridional distance increases.

It was found that the pressure distribution influences the optimum design. For a typical distribution that increases as the meridional distance increases, the gore width should be increased near the skirt for an optimum drag coefficient. Parameter studies show that by increasing the secondary structure flexibility the drag increases, although it is a secondary effect for present designs.

A well-known parameter in optimum parachute design is the suspension line length, and this study verifies that increasing the length improves the drag.

Optimum conditions are found by use of the maximum principle, steepest descent, and the Rayleigh-Ritz method.